Kinetics and Catalysis, Vol. 46, No. 2, 2005, pp. 227–250. Translated from Kinetika i Kataliz, Vol. 46, No. 2, 2005, pp. 243–268.
Original Russian Text Copyright © 2005 by Sadykov, Pavlova, Bunina, Alikina, Tikhov, Kuznetsova, Frolova, Lukashevich, Snegurenko, Sazonova, Kazantseva, Dyatlova, Usol'tsev, Zolotarskii, Bobrova, Kuz'min, Gogin, Vostrikov, Potapova, Muzykantov, Paukshtis, Burgina, Rogov, Sobyanin, Parmon.

Selective Oxidation of Hydrocarbons into Synthesis Gas at Short Contact Times: Design of Monolith Catalysts and Main Process Parameters

V. A. Sadykov, S. N. Pavlova, R. V. Bunina, G. M. Alikina, S. F. Tikhov, T. G. Kuznetsova, Yu. V. Frolova, A. I. Lukashevich, O. I. Snegurenko, N. N. Sazonova, E. V. Kazantseva, Yu. N. Dyatlova, V. V. Usol'tsev, I. A. Zolotarskii, L. N. Bobrova, V. A. Kuz'min, L. L. Gogin, Z. Yu. Vostrikov, Yu. V. Potapova, V. S. Muzykantov, E. A. Paukshtis, E. B. Burgina, V. A. Rogov, V. A. Sobyanin, and V. N. Parmon

Boreskov Institute of Catalysis, Siberian Division, Russian Academy of Sciences, Novosibirsk, 630090 Russia

Received April 1, 2004

Abstract—This review summarizes the main achievements of the Boreskov Institute of Catalysis (Siberian Division, Russian Academy of Sciences) in the development of efficient and stable monolith catalysts for selective oxidation of hydrocarbons into synthesis gas at short contact times. Research in this field has included (1) design of new types of active component based on metal oxides, (2) design of new types of monolith support and development of supporting procedures for active components, and (3) optimization of process parameters for different types of fuel (natural gas, isooctane, and gasoline) and oxidant (air oxygen, including its mixtures with water and carbon dioxide), including the start-up regime. Design of active components (platinum, nickel, or their combination) supported on fluorite-like solid solutions based on cerium dioxide and rare-earth (samarium, gadolinium, and praseodymium) or zirconium cations has been aimed at separating hydrocarbon activation (on metal sites) and oxidation (on the support) and conjugating the separated steps of hydrocarbon oxidation at the metal–oxide interface. Optimization of oxygen mobility in the support lattice by varying the nature and concentration of doping cation along with optimization of hydrocarbon activation on supported metal clusters allow hydrocarbons to be completely converted into synthesis gas by selective oxidation or dry or steam reforming at contact times of a few milliseconds, ruling out undesirable carbon build-up on the catalyst surface. The development of new types of monolith support has targeted the enhancement of thermal shock resistance, including testing of supports based on thermally stable metal foils and composites (cermets). The main steps of the production of these supports have been refined, including unique technologies of blast dusting and hydrothermal treatment. The electric conductivity of these systems allows a quick startup of selective oxidation to be performed by passing electric current, and their thermal conductivity minimizes the temperature gradient arising from heat transfer in the bed. Procedures for loading monolith supports with active components have been developed, including impregnation, washcoating, or encapsulation in cermet matrices. The catalysts produced show a high efficiency and an operational stability adequate to the above tasks in the selective oxidation and steam–air autothermal reforming of natural gas (including processes under pressure), isooctane, and gasoline into synthesis gas.

INTRODUCTION

At present, the selective oxidation and autothermal (steam–oxygen or steam–air) reforming of hydrocarbons into synthesis gas are considered to be promising alternatives to conventional steam reforming [1–5]. Special attention is given to the selective catalytic oxidation of methane, which is the main component of natural gas. Advantages of this process are mild exothermicity, superiority to steam reforming in terms of efficiency (productivity), and, hence, smaller reactor sizes (lower capital investments). The H_2 to CO ratio in synthesis gas obtained by selective methane oxidation is 2, which is most suitable for the Fischer–Tropsch syntheses of methanol and hydrocarbons. Therefore, the selective oxidation of natural gas is especially attractive for use at small pilot plants producing synthetic liquid fuel at remote deposits. Addition of water to an air–natural gas mixture (as in steam–air autothermal reforming) makes it possible to control the H_2 to CO ratio.

Synthesis gas can either be used as a fuel for high-temperature fuel cells or be converted into pure hydrogen through steam reforming and selective oxidation of CO. Therefore, catalytic converters of liquid and gaseous fuels into synthesis gas are the main units of both stationary and mobile energy installations based on low- and high-temperature fuel cells, which are the basis of future hydrogen power engineering. Small mobile fuel processors are feasible only with the selective oxidation of hydrocarbons into synthesis gas [5–7].

On-board synthesis gas generators on automobiles with internal combustion engines is of interest for the very near future. Due to the high diffusion rate and low

0023-1584/05/4602-0227 © 2005 MAIK "Nauka/Interperiodica"

ignition temperature of hydrogen, even the addition of small amounts of synthesis gas to gasoline can considerably improve the performance of an internal-combustion engine [8, 9]. The compression coefficient of the combustible mixture is substantially higher when hydrogen is burning in the engine. Furthermore, hydrogen broadens the inflammability range, allowing the use of gas mixtures that are leaner than are possible with any hydrocarbon fuel [8]. Thus, engine efficiency can be raised to 35–40% against 25–30% for a standard gasoline engine.Furthermore, hydrogen reduces fuel consumption and harmful emissions, particularly NO_x [10–12].

It is of great practical interest to add synthesis gas to ultra-lean feeds in the combustion chambers of turbines, for this allows one to stabilize combustion and reduce the nitrogen oxide content of exhaust to 1–5 ppm [13, 14].

In the general case, catalytic selective oxidation (autothermal reforming) of hydrocarbons into synthesis gas can be carried out in various types of reactors, including fixed-bed reactors with a granular catalyst, reactors with monolith catalysts, and fluidized-bed reactors [3, 15]. The most serious problems associated with local overheating of a catalyst arise when a fixed-bed reactor is used. In addition, this type of reactor has the largest overall dimensions, requiring the longest contact time τ. Heat and mass transfer in a fluidized bed can be intensified to flatten the temperature profiles and shorten τ. However, the design of such reactors (the presence of cyclones or related apparatuses) does not allow reduction in reactor dimensions. Inhomogenieties (bubbles) [3] can appear in the fluidized bed, resulting in oxygen slippage or soot formation. The shortest contact times (milliseconds) and, hence, small reactor dimensions are possible for selective oxidation on monolith catalysts, as demonstrated for the first time by Schmidt and his colleagues (University of Minnesota, the United States) [5]. However, only catalysts containing a large amount (up to 5 wt %) of rhodium, a rare and expensive metal, on a corundum support demonstrated stable performance and high efficiency in the selective oxidation of hydrocarbons into synthesis gas. At the same time, catalysts containing platinum and palladium (more available metals) were deactivated because of carbon buildup. These catalysts and processes are characterized by an almost complete consumption of the gas-phase oxygen in a thin (1- to 2-mm) inlet layer of the monolith, which has a high temperature up to 1200°C. In most of the monolith, the active component is in contact with a reaction mixture containing residual hydrocarbon and the products of its deep oxidation (H_2O, CO_2) and selective oxidation (CO, H_2). In the outlet region, where hydrocarbons undergo steam and dry reforming, some carbon buildup can occur on the surface. This either has no effect on the process (as in the case of rhodium) or inevitably deactivates the catalyst (as in the case of supported nickel, platinum, or palladium) [3, 5, 15]. This problem appears even in the selective oxidation of natural gas and is especially serious in the selective oxidation (steam–air autothermal reforming) of liquid fuels containing considerable amounts of naphthenes and aromatic compounds [16, 17]. In the inlet part of a monolith where high temperatures develop, undesirable processes of platinum oxide evaporation occur, leading to active component losses. Furthermore, several problems are associated with the specific behavior of ceramic monolith supports. For example, multiple on/off switches of a process bring about thermal shocks, causing cracking of corundum-based ceramic supports, which have a low thermal conductivity. The insufficient thermal conductivity of monolith ceramic supports leads to a slow heat transfer from the inlet zone, where heat is generated due to exothermic reactions, to the zone of endothermic reactions. This induces a high longitudinal temperature gradient in the monolith even under steady-state conditions.

The development of stable, highly efficient monolith catalysts for the processes considered is strongly impeded by the above-listed problems. This is among the reasons why these catalysts have not found industrial application. Obviously, solving these problems implies the development of new types of monolith support, search for cheaper and more stable active components, as well as the optimization of their composition and structure for different fuels and fundamentally different reaction conditions (compare the thin inlet layer, which is in contact with oxygen, and the main part of the monolith, where oxygen is absent).

Here, we survey the most important relevant results obtained at the Boreskov Institute of Catalysis (Siberian Division, Russian Academy of Sciences, Novosibirsk) in recent years [18–36]. Research in this field has resulted in the development of novel monolith catalysts, which have already been patented [37, 38] or are pending [39–45] in the Russian Federation.

One radical approach to the design of active components has been the replacement of the entire rhodium or most of it with platinum, a more available metal, including its combinations with nickel. The role of the metallic component is, primarily, the activation of the hydrocarbon molecule by homolytic cleavage of a C–H bond with the formation of hydrogen and hydrocarbon fragments adsorbed on metal particles [3–5, 46]. Further decomposition of these fragments on the metal surface, which leads to carbon buildup and loss of activity, can be prevented through their fast interaction with activated oxygen species migrating to the particle perimeter from the oxide support surface. The oxide support should be characterized by a high diffusion mobility of surface and lattice oxygen [47]. These properties possessed by mixed oxides are based on modified cerium dioxide [48], which are used as medium-temperature oxygen-conducting electrolytes [49] and reversible oxygen sources in automotive three-way catalysts [50]. In the ideal case, the mobility of oxygen in

the support lattice will be optimized taking into account the composition of the reaction mixture; this is in order to prevent both carbon buildup on the surface and a too rapid oxidation of the hydrocarbon fragments, which would lead to complete oxidation. The diffusion mobility and reactivity of lattice oxygen in solid solutions based on cerium dioxide or cerium–zirconium oxide solutions can be controlled by varying the concentration and nature of doping cation [49, 51].

Perovskites (mixed oxides containing reducible transition metal cations such as nickel, platinum, rhodium, ruthenium, and iridium and rare-earth cations such as lanthanum, yttrium, and praseodymium) are promising precursors for active components of catalysts for selective hydrocarbon oxidation into synthesis gas [21, 52, 53]. Metal clusters dispersed on the support surface (lanthanum hydroxocarbonate) form in a reductive reaction medium. It is shown that coke formation is suppressed on these catalysts owing to the basic properties of the support surface and that mobile hydroxyl groups or support-activated CO_2 molecules serve as a selective oxidant of hydrocarbon fragments in the absence of oxygen [54]. Since the properties of supported perovskite systems are described in detail in a number of publications and patents [18, 20, 21, 23, 37, 38], we will only touch on them here.

Monolith supports for the selective oxidation of hydrocarbons into synthesis gas within short contact times have been sought among the following types of support:

(1) thin-wall ceramic composite supports based on corundum and thermally stable oxide systems (partially stabilized zirconia, aluminum titanate, and titanium zirconate) produced by plastic paste extrusion [35, 36];

(2) honeycomb monoliths based on foils of thermally stable alloys, including those permitting heating by electric current for a rapid start-up [38, 43]; and

(3) microchannel supports based on heat-conducting cermets [39, 40].

The catalytic properties of the active components and monolith catalysts developed were tested in selective methane oxidation (including processes under pressure); steam–air, steam, and dry reforming of methane; and selective oxidation and steam–air autothermal reforming of isooctane and gasoline under both isothermal and autothermal (close to adiabatic) conditions in flow reactors at short contact times.

RESULTS AND DISCUSSION

1. Development and Properties of Active Components

The following problems have been addressed in the design of the active components based on fluorite-like ceria solid solutions doped with various cations:

(1) optimization of synthetic methods providing the most uniform spatial distribution of the dopant (lanthanum, samarium, gadolinium, and praseodymium cations) in the lattice of solid solutions based on cerium dioxide or CeO_2–ZrO_2 systems;

(2) elucidation of the influence of doping cations on the structural and surface characteristics of these systems;

(3) determination of factors controlling the mobility of surface and lattice oxygen in these systems and in the reactivity of this oxygen towards methane and its conversion products (hydrogen and CO); and

(4) study of the interaction in fluorite-like solid solution–supported platinum systems.

1.1. Structural characteristics

It has been established [19, 27] that, at doping Me(3+) or zirconium cation concentrations higher than 20–30 at. %, polymerized complex precursors (Pechini method [55]) afford a CeO_2-based single-phase solid solution with a rather uniform distribution of the doping cation over the thickness of the particles. At the same time, conventional methods of coprecipitation or decomposition of mixed salts (salt solutions) lead, as a rule, to the segregation of components, resulting in individual phases or microheterogeneous solid solutions [56]. The advantage of the Pechini method is that it produces a solid polymer matrix. This matrix consists of citric acid and ethylene glycol esters and has a statistically uniform distribution of both cerium and doping cations. Subsequent burnout of the organic matrix, producing hydroxocarbonate intermediates at moderate temperatures below 400°C, does not lead to a substantial mobility of cations. This explains why cations are only slightly segregated on the particle surfaces and at the intergrain boundaries and the resulting materials are single phases. In particular, this method can afford metastable cubic cerium dioxide–zirconium dioxide solid solutions containing 50 at. % zirconium [25], whereas conventional precipitation methods yield a mixture of cubic and tetragonal phases [57]. The lattice constant of the cubic solid solutions based on cerium dioxide varies in proportion to the concentration of the doping cation, indicating that this cation is uniformly distributed in the lattice [19]. A typical example is cerium dioxide containing gadolinium cations (Fig. 1). The particles of fluorite-like solid solutions consist of microdomains with characteristic sizes up to 150 Å (Fig. 1) stacked almost coherently to form larger plates with an almost perfect atomic structure (Fig. 2). As a rule, the size of these domains decreases with an increase in the concentration of the dopant (Fig. 1). Thus, this synthetic method produces nanodomain fluorite-like solid solutions. The specific surface area of multicomponent oxide solid solutions calcined below 700°C ranges between 20 and 100 m^2/g, indicating a rather small particle size.

As follows from the microdiffraction data (Fig. 2), the (111) face, which is characterized by the lowest surface energy, is the most developed in fluorite-like solid

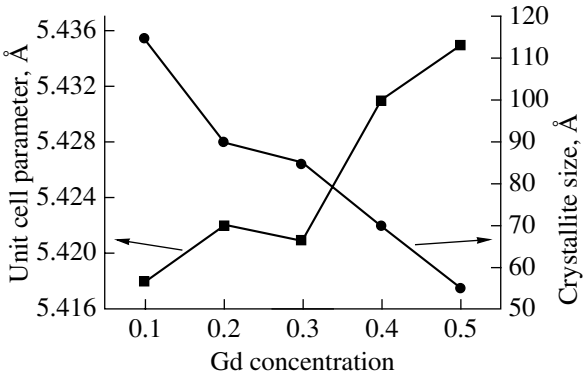

Fig. 1. Unit cell parameter of cerium dioxide synthesized by the Pechini method and crystallite size after calcination at 500°C as a function of Gd concentration in the solid solution.

solutions [58]. This face may have regular oxygen adsorption sites capable of forming M–O terminal species characterized by a heat of adsorption of ~60 kcal/mol [59]. This implies that oxygen on this surface possesses a moderate reactivity favoring the selective oxidation of hydrocarbons to synthesis gas.

WAXS, EXAFS, Raman spectroscopy, and lattice-mode IR spectroscopy data [30–33, 36] demonstrated that, even in the structure of pure cerium dioxide obtained by the Pechini method, oxygen polyhedra are tetragonally distorted, probably due to the residual anions (hydroxyl and carbonate groups) detected by IR spectroscopy. Introducing doping cations into the cerium dioxide lattice causes disorders in (distorts) the coordination sphere of all cations. This disorder shows itself as a decrease in the amplitude of corresponding peaks in the radial distribution curves and as splitting and weakening of the principal band in the Raman spectrum (Fig. 3). High dopant concentrations cause rearrangement of the structure (appearance of new coordination peaks), in particular, the formation of cluster defects including oxygen vacancy. This phenomenon, which decreases the ionic conductivity of ceria-based solid electrolytes as the concentration of a doping rare-earth cation is raised above the optimum content (10–20 at. %), is specific to these systems [49]. For samarium and gadolinium cations, whose radii are closest to the radius of Ce^{4+}, cluster formation is less pronounced than for larger cations of bismuth and lanthanum [49]. Evidently, it is defect clustering that causes the lanthanum-containing solid solution ($Ce_{0.5-x/2}Zr_{0.5-x/2}La_x$, $x = 0.1$–0.3) to decompose into two cubic solid solutions (with $a = 5.344$ and 5.479 Å for $CeZrLa_{0.3}$), which are likely to differ in lanthanum content [27].

1.2. IR spectroscopy of adsorbed CO

After CO adsorption at 77 K on the surface of pure cerium dioxide and doped ceria samples prepared by the Pechini method, we detected weak Lewis acid sites, including coordinately unsaturated M^{4+} cations (whose carbonyl complexes gave rise to absorption bands at 2160–2180 cm^{-1}) and M^{3+} cations (which revealed themselves as absorption bands at 2120–2130 cm^{-1} for low coverages) (Figs. 4 and 5). The latter cations were much less abundant, although they form a stronger bond with CO, as is suggested by the higher intensity of the corresponding band at low adsorbate coverages of the surface (Fig. 5). When the gaseous phase contains CO, absorption bands at 2090 and 2110 cm^{-1}, which are due to the dicarbonyl complexes of Ce^{3+}, are also observed [60]. This suggests that the absorption bands at 2120–2130 cm^{-1}, observed at low CO coverages of the surface, are due to the Ce^{3+} cations. In the case of cerium dioxide specimens promoted with praseodymium, which can readily change its oxidation state, the more complex shape of the spectrum (Fig. 6) suggests that some praseodymium cations are in the 3+ state and also can strongly bind CO at 77 K.

In the presence of CO in the gaseous phase, an intense band appears at 2146–2147 cm^{-1} (Figs. 4 and 6)

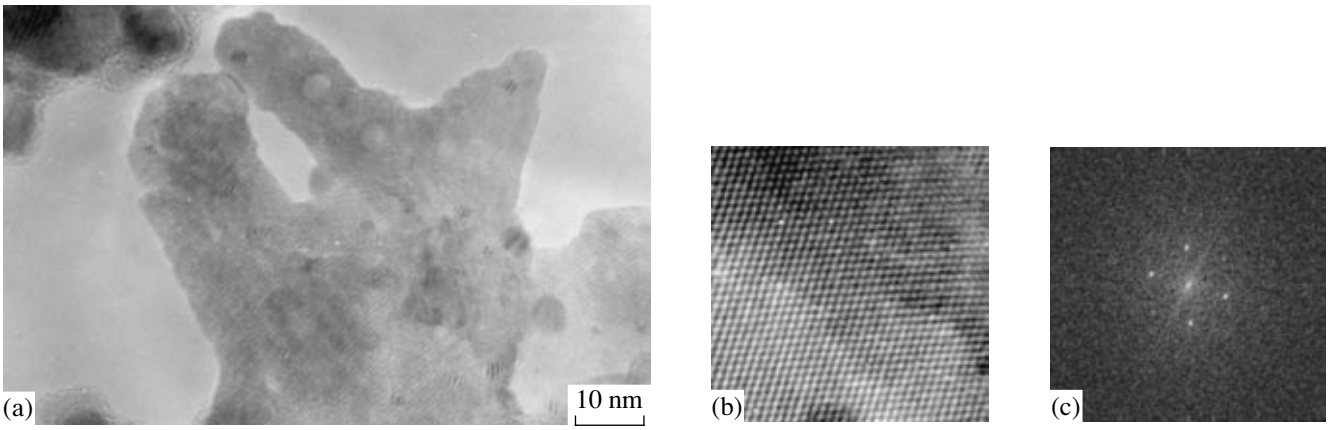

Fig. 2. (a) Typical view of particles of a fluorite-like solid solution based on cerium dioxide synthesized by the Pechini method, (b) high-resolution view of the lattice, and (c) its Fourier transform. $Ce_{0.5}Zr_{0.5}O_2$ system; calcination temperature, 700°C [27].

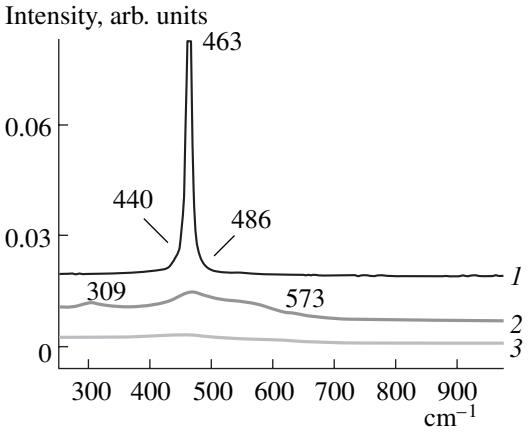

Fig. 3. Raman spectra of fluorite-like solid solutions: (*1*) CeO_2, (*2*) $Ce_{0.5}Zr_{0.5}$, and (*3*) $Ce_{0.35}Zr_{0.35}La_{0.3}O_x$.

due to CO complexes with surface hydroxyl groups. Since for all samples the region of stretching vibrations of the surface hydroxyl groups contains only absorption bands at 3630–3680 cm^{-1}, which are due to bridging hydroxyl groups (Fig. 7) [61], we believe that it is precisely these weakly acidic OH groups that form complexes with CO. The terminal hydroxyl groups (absorption bands at 3780 cm^{-1}) [61] are absent or are present in very small amounts.

For cerium dioxide doped with triply charged cations, the concentration of coordinately unsaturated Ce^{4+} cations passes through a maximum at a low dopant concentration. This is demonstrated for the CeO_2–Gd system (Fig. 8). Study of the defect structure and electric conductivity of doped ceria showed that the concentration of nonassociated oxygen vacancies is highest in this composition region [49]. Comparison of these results with our data suggests that the concentration of surface oxygen vacancies correlates with the concentration of free (nonassociated) anionic vacancies in the lattice. The tendency of triply charged cations to segregate both on the surface and at the domain boundaries of cerium dioxide particles can contribute to the decrease in the concentration of oxygen vacancies on the surface [62]. This tendency also favors surface restructuring, decreasing the concentration of oxygen vacancies. At the same time, the concentration of the coordinately unsaturated Ce^{3+} cations changes to a much lesser extent and does not correlate with the concentration of free anionic lattice vacancies (Fig. 8). Furthermore, no dependence of the concentration of Brønsted acid sites on dopant content is observed. It is not impossible that most of the coordinately unsaturated

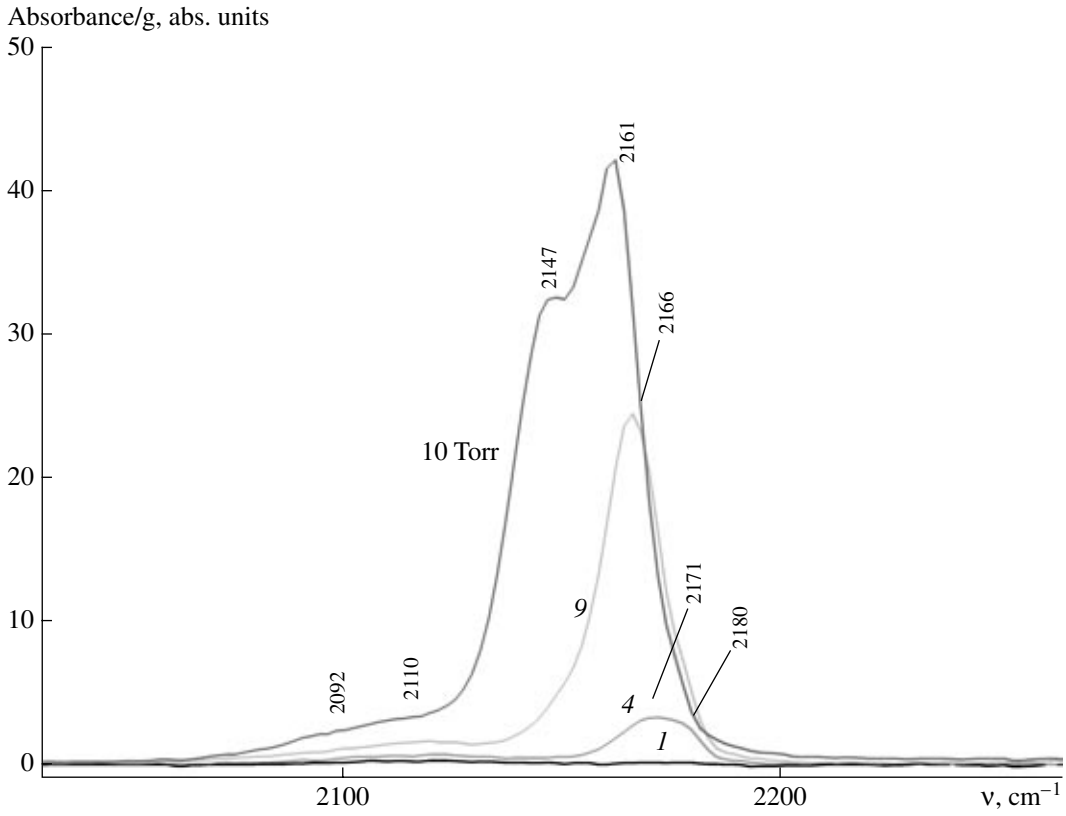

Fig. 4. IR spectra of CO adsorbed at 77 K on $Ce_{0.8}Gd_{0.2}O_{2-x}$ surface. The spectra were recorded after (*1*) 1, (*4*) 4, and (*9*) 9 doses of CO were added to the cell (one dose is 4 μmol of CO) and after a CO pressure of 10 Torr was established in the cell. Treatment conditions: 1 h under 10 Torr O_2 (400°C) and pumping at the same temperature.

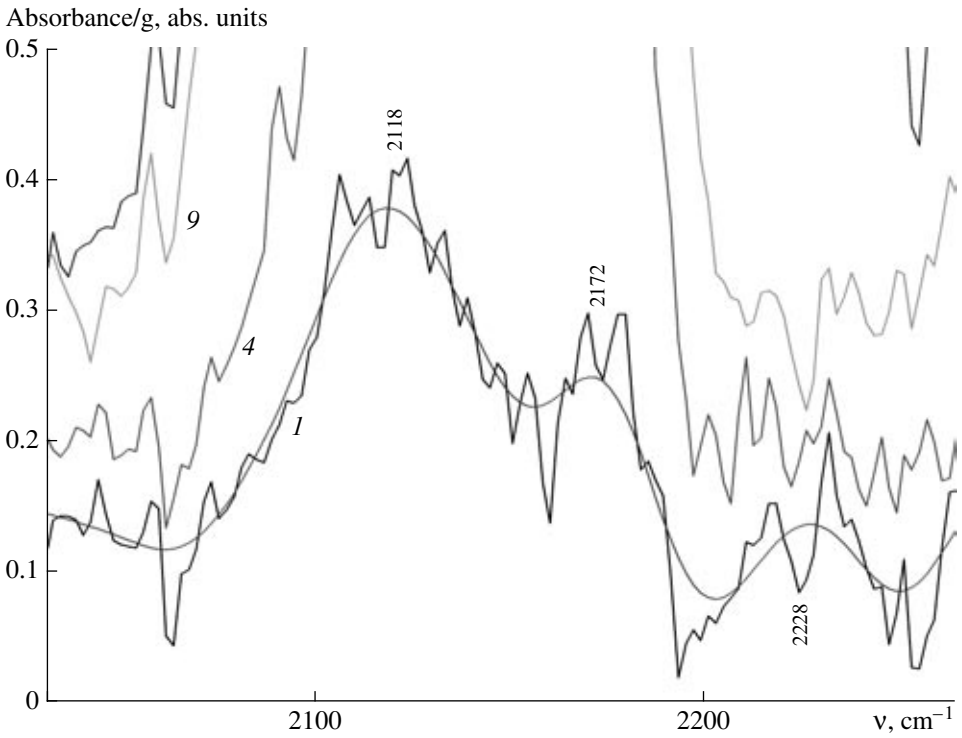

Fig. 5. IR spectra of CO adsorbed at 77 K on $Ce_{0.8}Gd_{0.2}O_{2-x}$ surface. The spectrum recorded after the first dose of CO was adsorbed is marked out. Sample treatment conditions and curve numbering are the same as in Fig. 4.

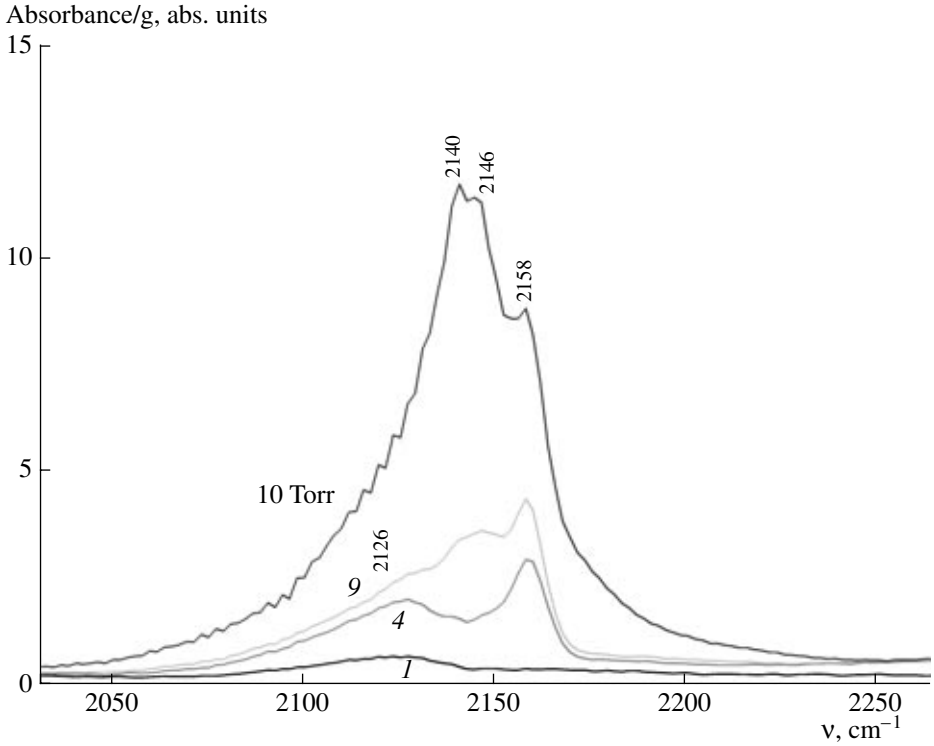

Fig. 6. IR spectra of CO adsorbed at 77 K on $Ce_{0.9}Pr_{0.2}O_{2-x}$. Sample treatment conditions and curve numbering are the same as in Fig. 4.

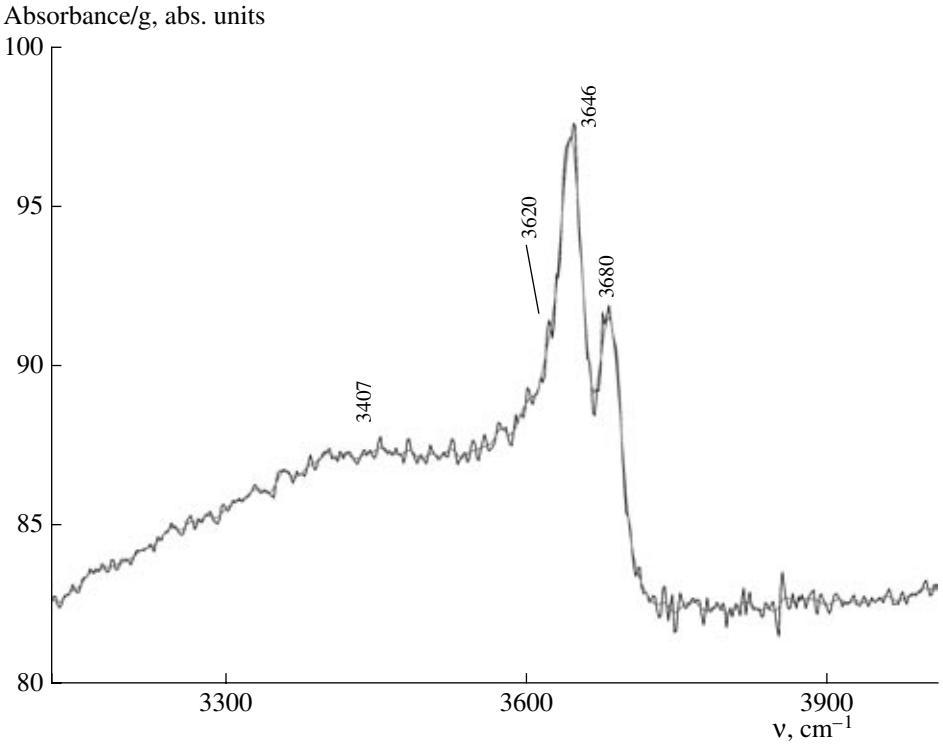

Fig. 7. IR spectra in the region of stretching vibrations of hydroxyl groups at 77 K for $Ce_{0.8}Gd_{0.2}O_{2-x}$.

Ce^{3+} cations (as well as most of the hydroxyl groups, most likely) are located at domain boundaries, whose concentration increases with an increase in the doping cation concentration, thus compensating for the decrease in the concentration of oxygen vacancies in the lattice.

For the more complex system Ce–Zr–La–O, the incorporation of lanthanum cations into the lattice, which must generate anionic vacancies according to the principle of electric neutrality, also decreases the concentration of coordinately unsaturated surface M^{4+} cations (Fig. 9), most likely through restructuring. Indeed, when the lanthanum content of this system increases, absorbance in the visible region decreases, which can be ascribed to isolated anionic vacancies (Ce^{3+} cations) (Fig. 10). However, at a lanthanum content corresponding to $x = 0.3$, the concentration of the coordinately unsaturated surface M^{4+} cations increases again (Fig. 9), probably due to the heterogeneous character of the system. It should be noted that the absorption band at 2130 cm^{-1}, which corresponds to the CO complexes with coordinately unsaturated M^{3+} cations, disappears after lanthanum is introduced. This suggests that lanthanum cations are partially segregated in the vicinity of domain boundaries, where these coordinately unsaturated cations can exist, and are blocked as a result. Furthermore, the lanthanum-containing samples are characterized by a systematic low-frequency shift of the absorption band corresponding to CO complexes with Lewis acid sites (M^{4+} cations, primarily, Zr^{4+}) (Fig. 9). This means a decrease in the strength of these Lewis acid sites.

In the general case, for all platinum-supported doped ceria samples, IR spectra exhibit absorption bands at 2050 cm^{-1} corresponding to terminal CO adsorption species on metallic platinum (Fig. 11). It was found that the concentration of both Brønsted and Lewis acid sites decreases upon supporting of platinum and/or nickel. The bands corresponding to CO com-

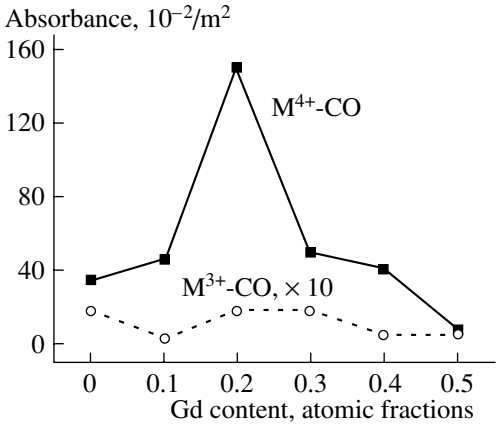

Fig. 8. Normalized intensity of the absorption bands due to CO complexes with coordinately unsaturated surface sites M^{4+} (36 μmol of adsorbed CO) and M^{3+} (4 μmol of adsorbed CO) versus gadolinium content.

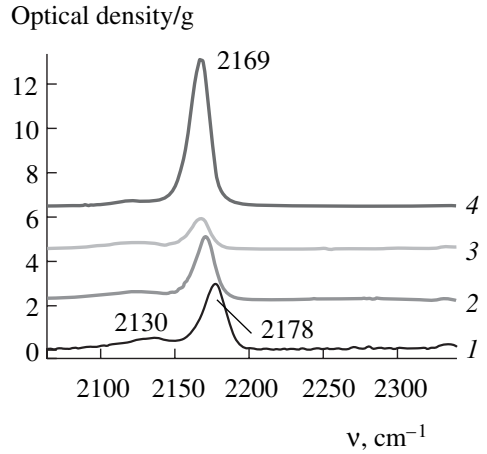

Fig. 9. IR spectra of CO (16 μmol) adsorbed at 77 K on $Ce_{0.5-x/2}Zr_{0.5-x/2}La_x$ samples: x = (*1*) 0, (*2*) 0.1, (*3*) 0.2, and (*4*) 0.3.

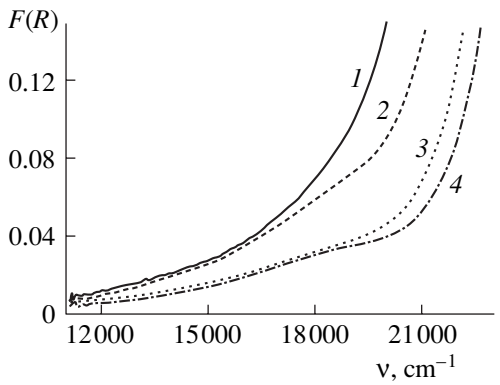

Fig. 10. Diffuse reflectance electronic spectra in the visible region for $Ce_{0.5-x/2}Zr_{0.5-x/2}La_x$ samples: x = (*1*) 0, (*2*) 0.1, (*3*) 0.2, and (*4*) 0.3.

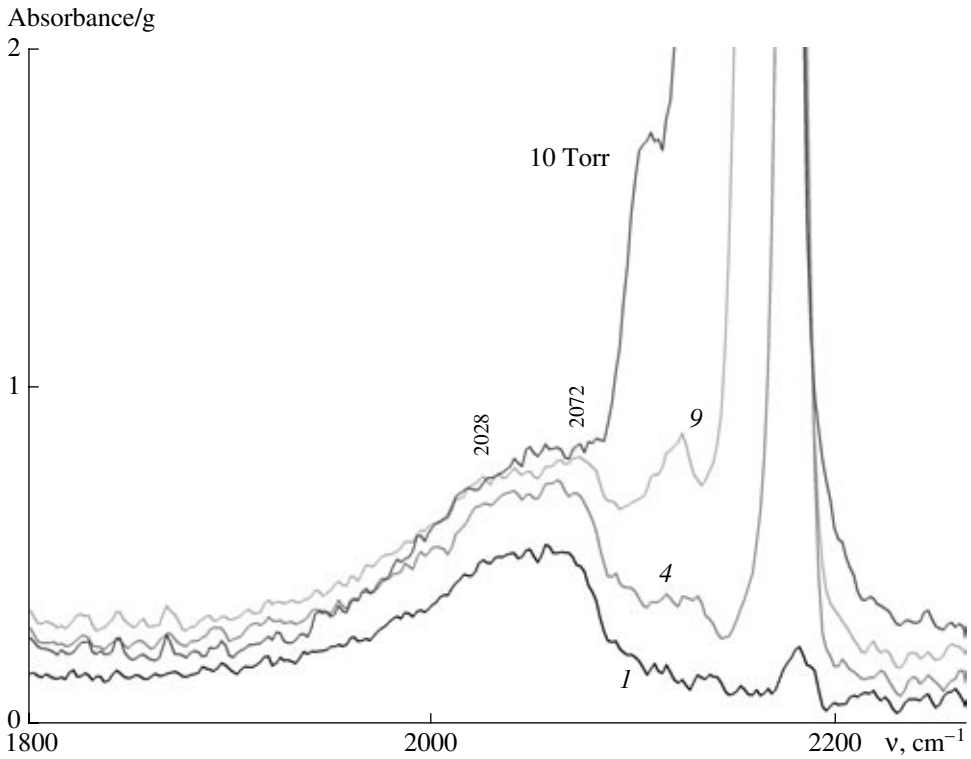

Fig. 11. IR spectra of CO adsorbed at 77 K on 1.4 wt % $Pt/Ce_{0.8}Gd_{0.2}O_{2-x}$. Sample treatment conditions and curve numbering are the same as in Fig. 4.

plexes with coordinately unsaturated M^{3+} cations, which are probably located at domain boundaries, almost disappear (Fig. 11). This implies that platinum clusters are anchored by the surface acid sites and, most likely, primarily in the vicinity of disordered domain boundaries. However, supports still differ in the concentration of coordinatively unsaturated M^{4+} cations after platinum is supported (Fig. 12). In turn, the intensity of absorption bands corresponding to the Pt^0–CO complexes (e.g., the absorption band at 2050 cm^{-1}) also varies from sample to sample and is generally independent of the starting concentration of weak Lewis acid sites on the surface (M^{4+} cations). Indeed, on the one hand, at excessively high defect concentrations on the surface and strong platinum–support interaction, oxidized platinum species can be incorporated into the

near-surface layer, decreasing the number of platinum atoms accessible to CO [62]. In particular, even for a rather high platinum content (1.4 wt %), only a relatively small number of platinum clusters on the surface of fluorite-like supports can be observed by electron microscopy (see, e.g., Fig. 2). On the other hand, for a small number of stabilization sites, platinum atoms can aggregate to form rather large particles with a relatively small number of surface platinum atoms.

1.3. Reactivity and diffusion mobility of oxygen in fluorite-like oxide solid solutions

1.3.1. Oxygen isotope heteroexchange [28, 30, 31, 34]. Third type heteroexchange is typical of fluorite-like oxide systems (two surface oxygen atoms are involved in the exchange [63]). The activation energy of this process is ~80 kJ/mol, and the order with respect to oxygen in the pressure region examined (100–300 Pa) is close to 0.5. Some data for the systems studied are presented in the table.

In temperature-programmed runs for cerium dioxide containing samarium or gadolinium cations [64], the amount of exchangeable oxygen passes through a maximum (X_e ~ 2 monolayers) at a relatively low degree of substitution (x = 0.2) and correlates with the concentration of isolated (free) oxygen vacancies both in the lattice and on the surface (see above). An increase in the degree of substitution usually results in a systematic, although comparatively small (100 to 150°C), shift of the onset point of intensive heteroexchange (400°C) to higher temperatures. Although lanthanum–cerium–zirconium samples have a higher density of surface defects, the heteroexchange rate and amount of exchangeable oxygen for these samples are lower than for cerium dioxide samples containing samarium or gadolinium. These results suggest that the heteroexchange reaction in the temperature region examined (above 400°C) is controlled by oxygen mobility in the lattice (concentration of isolated cationic vacancies) rather than by the surface reaction itself [64]. This assumption is consistent with the fact that the introduction of platinum into the Ce–Zr–O system exerts a weak effect on the exchange rate but increases the amount of exchangeable oxygen (table). This specific feature can be due to platinum incorporating into the surface layer and activating oxygen atoms [19].

1.3.2. Reduction with hydrogen and carbon monoxide. The incorporation of dopants into cerium dioxide shifts the main reduction peak corresponding to oxygen removal from the lattice from ~800 to 500–550°C (Figs. 13–15). It is most likely that the additive sharply increases oxygen mobility in the CeO_2 lattice so that the reduction process is controlled by hydrogen activation on the oxide surface. The disappearance of the high-temperature peak at high concentrations of the dopant, regardless of its nature or charge, indicates disordering of the whole oxide lattice, in accordance with structural

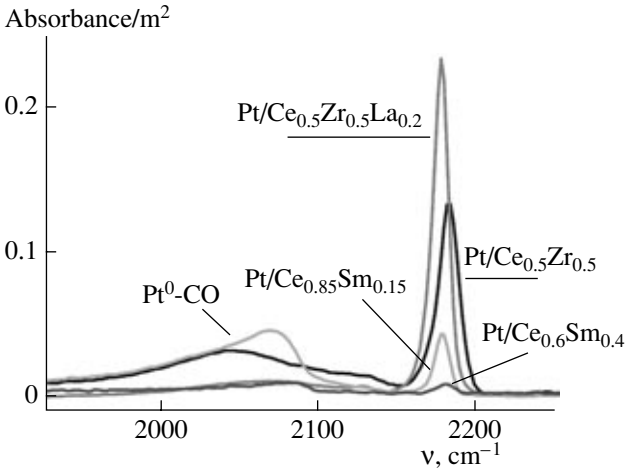

Fig. 12. IR spectra of CO adsorbed at 77 K on fluorite-like solid solutions promoted with platinum. The spectra were recorded after 16 μmol of CO were adsorbed.

data (see above). Note that the total amount of lattice oxygen removed with hydrogen is at most two monolayers. Therefore, it is quite possible that near-surface layers are primarily reduced in these experiments. This agrees with the fact that a diffusion-controlled plateau is observed in the reduction curves up to very high temperatures when the amount of oxygen removed is comparable with that corresponding to the main temperature-programmed reduction (TPR) peak. As would be expected, the total amount of oxygen removed with hydrogen from samples containing nonreducible cations in the temperature-programmed mode below 900°C decreases systematically with decreasing molar fraction of cerium. Moreover, the highest reduction rate, which characterizes oxygen mobility in the lattice, passes through a maximum at low degrees of substitution (Fig. 16), correlating with the concentration of free oxygen vacancies in the lattice. Since in this region the concentration of surface Lewis acid sites capable of activating hydrogen also passes through a maximum, it is not impossible that the maximum reactivity of the samples with a low dopant content is determined solely by surface phenomena.

Oxygen isotope heteroexchange on fluorite-like samples

Sample	T, K	P, Pa	X_e^*	$R \times 10^{-15}$, O_2 molecules m^{-2} s^{-1}**
$Sm_{0.2}Ce_{0.8}O_{1.9}$	723	140	7	1.4
$Ce_{0.5}Zr_{0.5}O_2$	773	140	1	1.5
$Pt/Ce_{0.5}Zr_{0.5}O_2$	773	110	7	2.4

* Amount of exchangeable oxygen (monolayers).

** Heteroexchange rate.

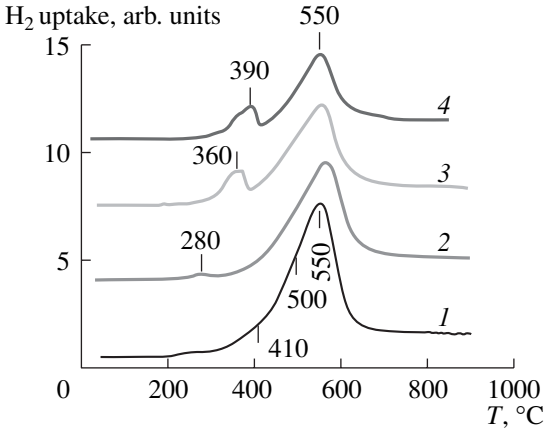

Fig. 13. Hydrogen TPR curves for $Ce_{0.5 - x/2}Zr_{0.5 - x/2}La_x$ samples: x = (*1*) 0, (*2*) 0.1, (*3*) 0.2, and (*4*) 0.3. The samples are pretreated with O_2 at 400°C for 1 h. The heating rate is 10 K/min. H_2 uptake, 10^{-4} mol/g: (*1*) 15.7, (*2*) 13.0, (*3*) 11.4, and (*4*) 9.8.

For high concentrations of nonreducible cations in fluorite-like ceria-based solid solutions, small peaks appear in the TPR curves between 200 and 400°C (Figs. 13–15). They most likely correspond to the removal of the most reactive oxygen species from a small part of the reconstructed surface (see above). However, it should be mentioned that these features are not observed for the isothermal reduction of the samples with carbon monoxide in a similar temperature range (Fig. 17), when the reduction rates also correlate mainly with the total amount of reactive oxygen in the sample.

For the praseodymium-containing samples, the situation is fundamentally different: the rate of reduction with hydrogen and the total amount of oxygen removed in the TPR mode increase with increasing dopant content (Fig. 16). Unlike, for example, the samples of the cerium–gadolinium series, praseodymium-containing sample show no pronounced correlation between reduction rate and the concentration of surface Lewis acid sites. This implies that the activation of hydrogen molecules directly involves reactive oxygen located on praseodymium cations. Note that the maximum achievable rate of oxygen removal from the lattice of samples with triply charged cations (for instance, gadolinium) exceeds the maximum rate for the samples of the cerium–praseodymium series, although praseodymium is more readily reducible. This suggests that the maximum rate of oxygen removal from these samples is also dependent on the concentration of free oxygen vacancies in the lattice. At the same time, the high rate of bulk reduction for the ceria–zirconia system is evidently due to the marked distortion of the coordination sphere of the zirconium cations rather than to free anionic vacancies. This distortion generates defects of the interstitial oxygen atom–oxygen vacancy type [65] and, as a result, mobile oxygen atoms in the lattice [66].

The shift of the middle-temperature peaks of the temperature-programmed hydrogen reduction of the platinum-containing samples from 500 to 200–300°C is not accompanied by a substantial change in the amount of oxygen released or in the positions of high-temperature peaks for samples with a low concentration of doping cations (Figs. 18, 19). Undoubtedly, the observed low-temperature shift is due to the more efficient activation of a hydrogen molecule on metallic platinum as compared to hydrogen activation on surface Lewis acid sites. At the same time, the abiding correlation between reduction rates for both platinum-promoted and unpromoted samples of one series (compare

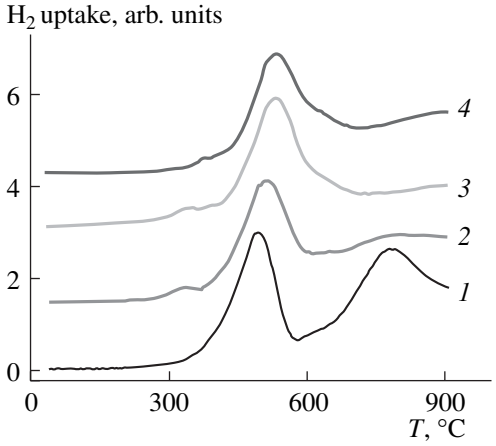

Fig. 14. Hydrogen TPR curves for cerium–gadolinium oxide samples: (*1*) $Gd_{0.1}Ce_{0.9}O_y$, (*2*) $Gd_{0.2}Ce_{0.8}O_y$, (*3*) $Gd_{0.4}Ce_{0.6}O_y$, and (*4*) $Gd_{0.5}Ce_{0.5}O_y$. The samples are pretreated with O_2 at 400°C for 1 h. The heating rate is 10 K/min.

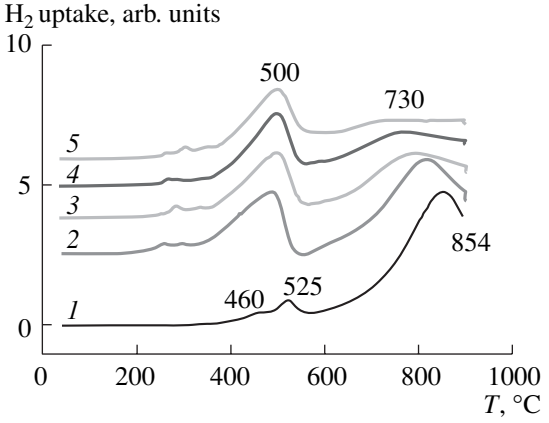

Fig. 15. Hydrogen TPR curves for cerium–samarium oxide samples: (*1*) CeO_2, (*2*) $Ce_{0.95}Sm_{0.05}$, (*3*) $Ce_{0.9}Sm_{0.1}$, (*4*) $Ce_{0.85}Sm_{0.15}$, and (*5*) $Ce_{0.8}Sm_{0.2}$. The samples are pretreated with O_2 at 400°C for 1 h. The heating rate is 10 K/min. H_2 uptake, 10^{-4} mol/g and (number of monolayers): (*1*) 10.9 (3.4), (*2*) 9.6 (1.0), (*3*) 9.2 (1.6), (*4*) 9.9 (1.3), and (*5*) 8.0 (0.6).

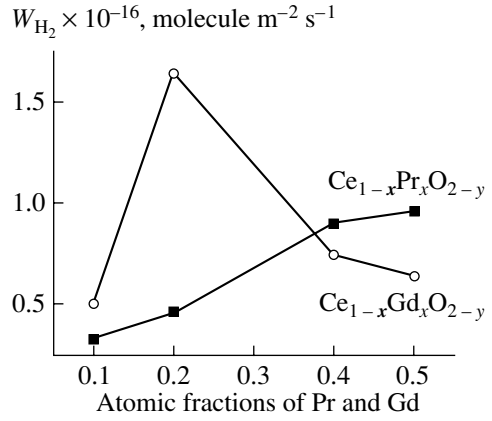

Fig. 16. Maximum specific rate of reduction with hydrogen (peak at 500°C) versus praseodymium and gadolinium concentrations in CeO_2.

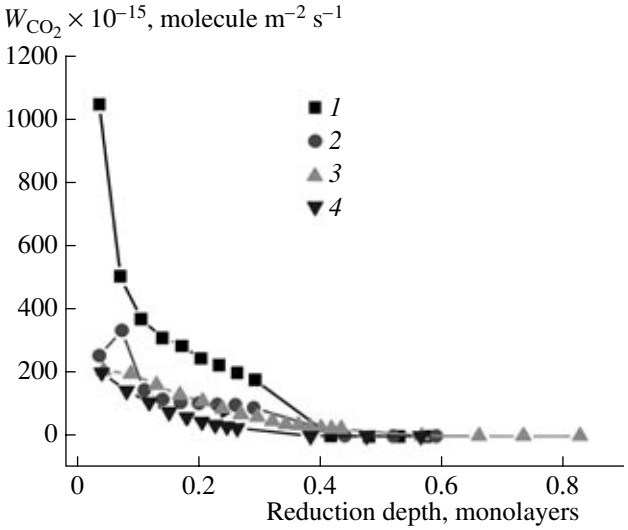

Fig. 17. Reduction rates of the cerium–zirconium oxide solid solutions $Ce_{0.5-x/2}Zr_{0.5-x/2}La_x$ with x = (*1*) 0, (*2*) 0.1, (*3*) 0.2, and (*4*) 0.3 versus reduction depth (500°C, 1% CO in helium, treatment in O_2 for 1 h at 500°C).

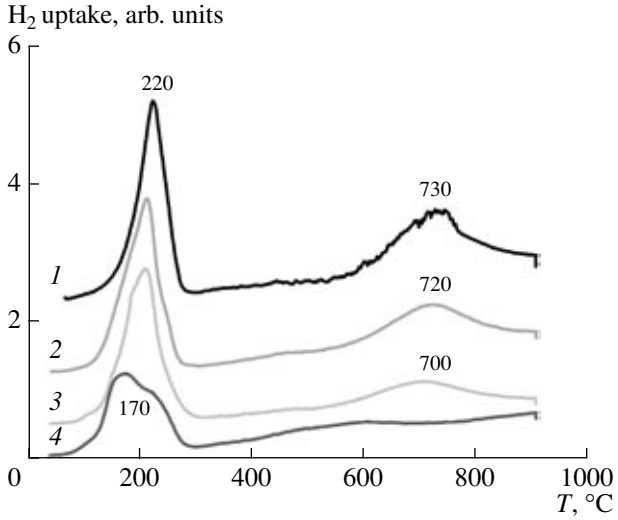

Fig. 18. Hydrogen TPR curves for platinum-promoted (1.4 wt % Pt) samples of the cerium–samarium oxide system $Pt/Ce_{1-x}Sm_x$: x = (*1*) 0.05, (*2*) 0.1, (*3*) 0.15, and (*4*) 0.4. The samples are pretreated with O_2 at 400°C for 1 h. The heating rate is 10 K/min. H_2 uptake, 10^{-4} mol/g and number monolayers: (*1*) 11.6 (1.2), (*2*) 12.8 (1.6), (*3*) 10.1 (1.4), and (*4*) 10.0 (1.5).

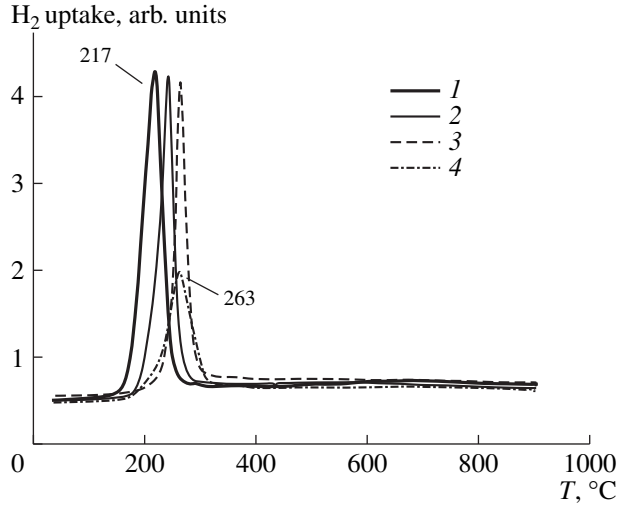

Fig. 19. Hydrogen TPR curves for platinum-promoted (1.4 wt % Pt) samples of the cerium–zirconium oxide system containing lanthanum: (*1*) $Pt/Ce_{0.5}Zr_{0.5}$, (*2*) $Pt/Ce_{0.45}Zr_{0.45}La_{0.1}$, (*3*) $Pt/Ce_{0.4}Zr_{0.4}La_{0.2}$, and (*4*) $Pt/Ce_{0.35}Zr_{0.35}La_{0.3}$. The samples are pretreated with O_2 at 400°C for 1 h. The heating rate is 10 K/min.

Figs. 15 and 18) indicates that the maximum rate itself is determined by oxygen mobility in the lattice. Evidently, the high-temperature TPR peaks persisting in the platinum-promoted samples with a low dopant content also correspond to the topochemical reduction of that part of the cerium dioxide lattice that contains no doping cations and related anionic vacancies.

1.3.3. Reduction with methane. Initially, at lower temperatures, TPR with methane results in the complete oxidation of CH_4. The products of selective oxidation (hydrogen and CO) form at higher temperatures, after reactive oxygen species are removed (Figs. 20, 21). The existence of several peaks in the reduction curves indicate that the reduction process involves different oxygen species and is accompanied by structural changes in the fluorite-like solid solution. Since, according to oxygen balance data, all Ce^{4+} cations are reduced to Ce^{3+} in the temperature range examined, this restructuring must finally result in a pyrochlore structure [57]. Indeed, an electron micrograph of particles of the fluorite-like solid solution subjected to

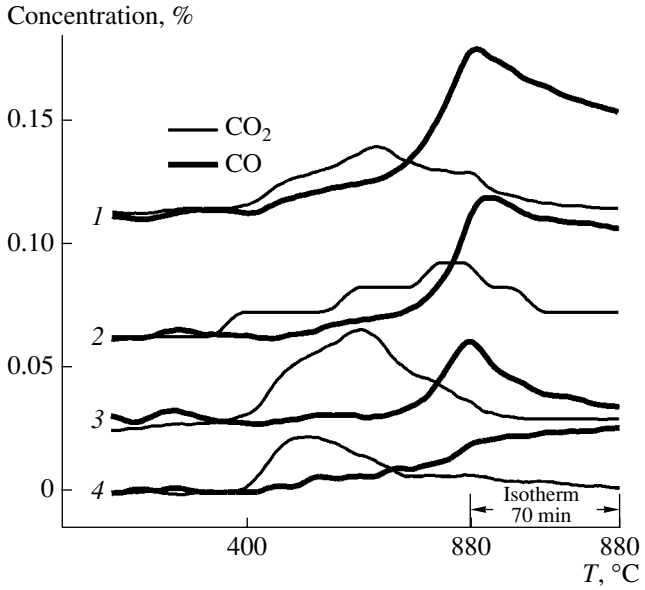

Fig. 20. Methane TPR curves (1% CH_4 in He) for $Ce_{1-x}Gd_xO_{2-y}$ samples: x = (*1*) 0.1, (*2*) 0.2, (*3*) 0.4, and (*4*) 0.5. The heating rate is 5 deg/min. The products are continuously analyzed using a PEM-2M gas analyzer.

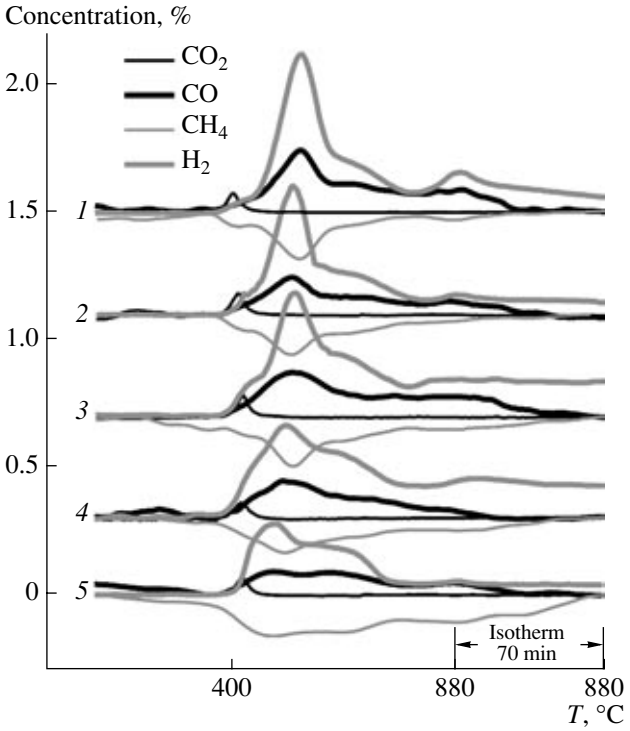

Fig. 21. Methane TPR curves (1% CH_4 in He) for samples of the platinum-promoted (1.4 wt % Pt) cerium–gadolinium series $Pt/Ce_{1-x}Gd_xO_{2-y}$: x = (*1*) 0.1, (*2*) 0.2, (*3*) 0.3, (*4*) 0.4, and (*5*) 0.5. The heating rate is 5 K/min. The products are continuously analyzed using a PEM-2M gas analyzer.

deep methane reduction shows both a developed domain structure and moire patterns indicating a superposition of lattice regions with similar structural characteristics (compare, e.g., Fig. 22 for the platinum-promoted cerium–zirconium oxide system and Fig. 2 for the original sample).

For the methane reduction of cerium dioxide samples containing samarium, gadolinium, and praseodymium cations, the strongest CO_2 evolution peaks shift to the low-temperature region as dopant concentration is increased (see, e.g., Fig. 20). This is evidently due to the formation of more reactive oxygen species, which were observed as small peaks at 300–400°C in hydrogen TPR (see above). Note that the maximum rate of methane oxidation to CO_2 and CO and the maximum rate of hydrogen oxidation depend on doping cation content in similar ways (compare Figs. 23 and 16). In the general case, the selectivity of formation of partial methane oxidation products on cerium dioxide samples containing triply charged cations is substantially higher than that in the presence of the CeO_2–Pr system (see, e.g., Fig. 23). Likewise, incorporation of lanthanum cations into a ceria–zirconia solid solution suppresses complete oxidation.

Supporting of platinum onto the surface of fluorite-like oxide systems substantially enhances their reactivity towards methane: the formation peaks of the products of both complete and selective oxidation shift to lower temperatures. Furthermore, the selectivity of formation of partial oxidation products increases (Fig. 21). These results indicate a sharp increase in the activation rate of methane molecules related to the easy cleavage of C–H bonds on metallic platinum. In this case, the onset of methane reduction of the platinum-modified systems at relatively low (~400°C) temperatures is generally accompanied by both complete and deep oxidation and by rapid disappearance of the deep oxidation products. This suggests a parallel–consecutive reaction mechanism [3, 71] possibly including CO and hydro-

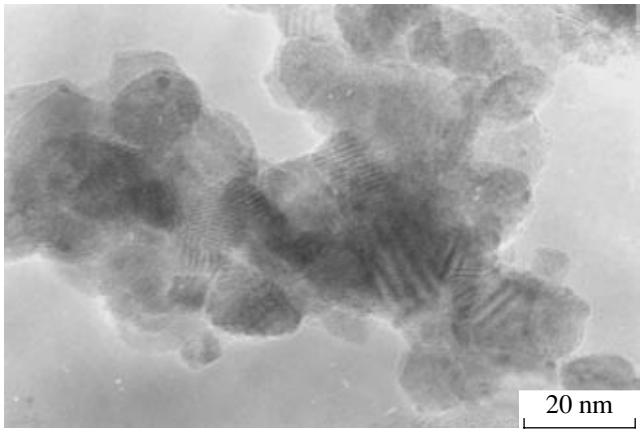

Fig. 22. Typical view of particles of the cerium–zirconium oxide system after deep reduction with methane.

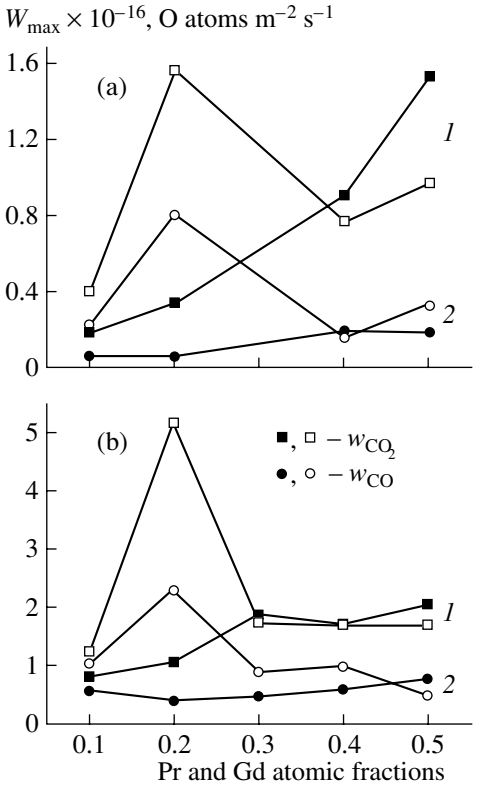

Fig. 23. Maximum rates of lattice oxygen consumption in complete oxidation ($CO_2 + H_2O$) and selective oxidation ($CO + H_2$) versus doping cation content for (a) unpromoted and (b) platinum-promoted samples of the (light points) cerium–gadolinium ($Ce_{1-x}Gd_xO_{2-y}$) and (dark points) cerium–praseodymium ($Ce_{1-x}Pr_xO_{2-y}$) series.

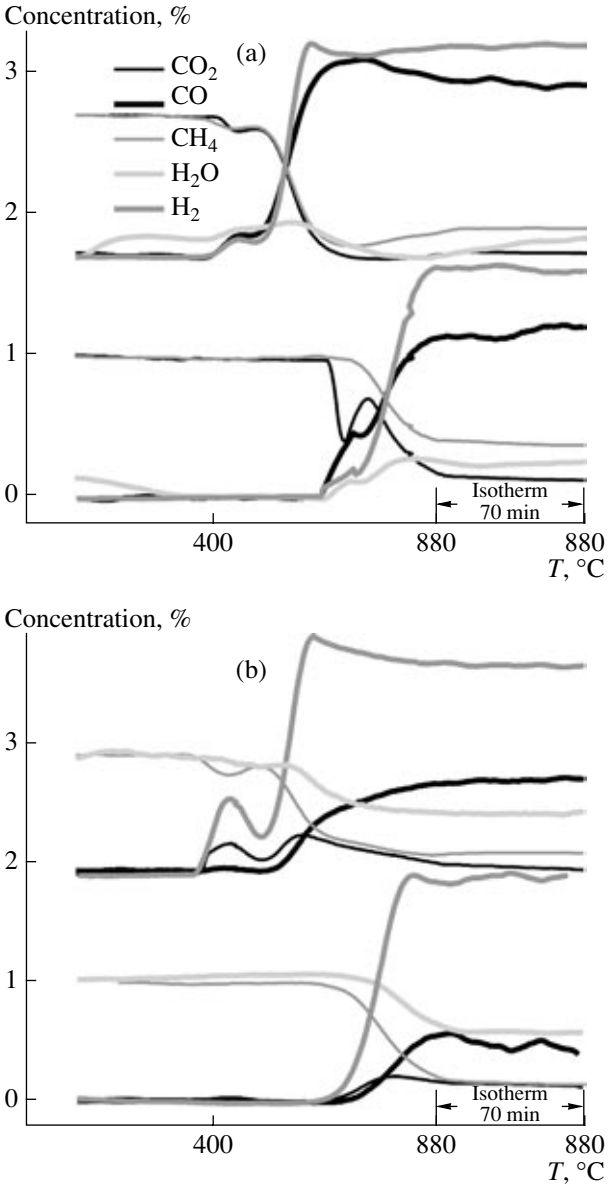

Fig. 24. Temperature-programmed reaction data for (a) dry and (b) steam reforming of methane on platinum-promoted samples of the cerium–gadolinium series $Gd_{0.2}Ce_{0.8}O_{2-y}$ after the (upper curves) oxygen treatment and (lower curves) TPR with methane. The space velocity is 50000 h^{-1} (contact time, 108 ms).

gen after-oxidation involving relatively weakly bound oxygen species on defect sites on the surface of the fluorite-like solid oxide solution. For deep reduction of the samples, a decrease in the rate of oxygen migration from the oxide particle bulk to the surface stops CO formation. At the same time, stable hydrogen formation is observed (Fig. 21), indicating accumulation of coke deposits on the catalyst surface. In accordance with these results, CO_2 and H_2O are formed during the temperature-programmed reoxidation of the samples that have been reduced with methane, and the amount of carbon thus detected does not exceed 1% of the total amount of methane converted.

Although supported platinum causes dramatic changes both in the selectivity of formation of partial oxidation products and in reduction temperature, the intrinsic dependence of the maximum rates of oxygen consumption in complete and selective oxidation reactions on doping cation content is retained (Fig. 23). Supported platinum increases the maximum rates by a small factor of 2 to 3. These results suggest that the maximum rates of complete and partial oxidation are determined, to a great extent, by the diffusion mobility of both surface and lattice oxygen even for the platinum-promoted systems. At the same time, comparing the results for the sample series containing gadolinium and praseodymium demonstrates that the selectivity of formation of complete and selective oxidation products clearly depends on the composition and specific features of the defect structure of the surface of complex oxide systems. An increase in the concentration of surface defects, the oxidizing power of the surface, and mobility of surface oxygen favors an increase in the selectivity of formation of complete oxidation products. However, as follows from the data presented in

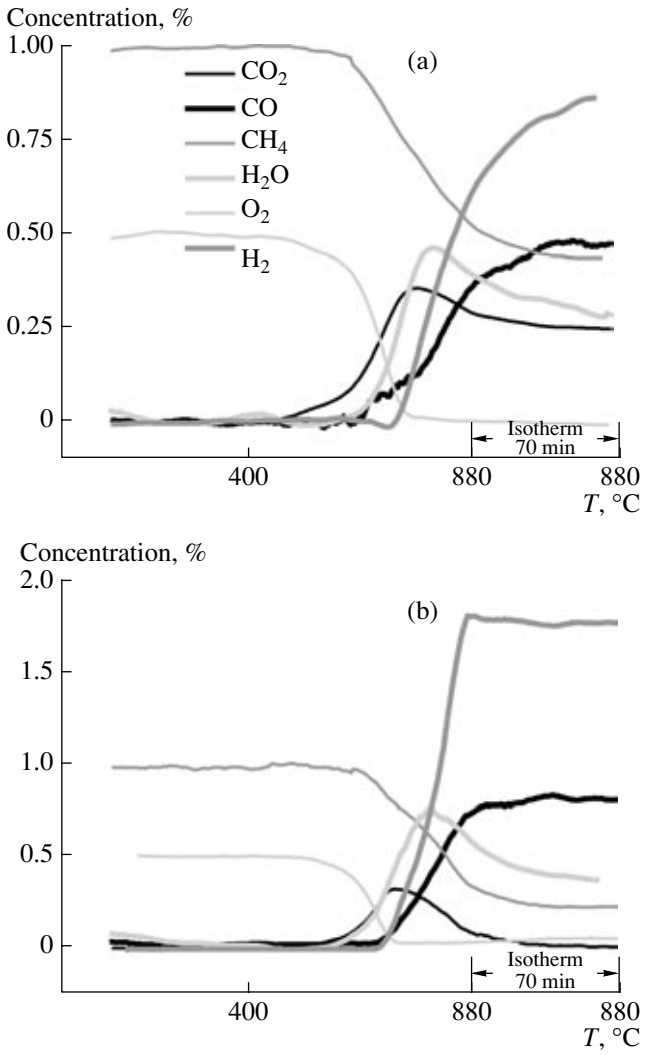

Fig. 25. Temperature-programmed reaction data for selective oxidation of methane on the platinum promoted samples (a) $Ce_{0.8}Gd_{0.2}O_{2-x}$ and (b) $Ce_{0.6}Gd_{0.4}O_{2-x}$ after oxygen treatment. The contact time is 5 ms, and the heating rate is 5 K/min.

Fig. 21, for the methane TPR of the platinum-promoted samples, the above conclusion mainly refers to the oxidized state of the surface, because synthesis gas is formed with 100% selectivity at $T > 450$°C after reactive oxygen is removed. Nevertheless, these differences do appear in the case of selective oxidation of methane with oxygen at millisecond contact times (see below).

1.3.4. Steam and dry reforming processes. Since these processes can occur parallel to selective methane oxidation to synthesis gas even at short contact times [67, 68], it is important to observe how the activity of the above metal oxide systems in these reactions depends on the properties of the support. These experiments were carried out on both fresh (O_2-treated) platinum-containing catalysts and on catalysts subjected to methane TPR. Stoichiometric reaction mixtures were used (1% CH_4 + 1% H_2O or 1% CH_4 + 1% CO_2 in helium) whose compositions were similar to the compositions that may be observed in most monolith catalysts during selective hydrocarbon oxidation to synthesis gas at short contact times.

The most typical results for a platinum-promoted sample of the cerium–gadolinium system are presented in Fig. 24. As follows from the data presented, on the oxidized samples the reforming reaction starts at 400–500°C, after removal of the active oxygen species from the surface. Deep reduction by methane at 880°C, accompanied by partial sintering of the active component and carbon build-up, shifts the onset temperature of catalyst operation to 600–650°C. However, regardless of sample treatment conditions, the equilibrium conversion of methane is achieved at 880°C. The high efficiency of platinum/fluorite-like oxide catalysts with a high oxygen mobility in steam and dry reforming is in agreement with the results obtained for similar systems by other researchers [67, 68].

1.3.5. Selective oxidation of methane into synthesis gas at millisecond contact times. *Bulk samples.* In our experiments, we used catalyst beds up to 25 mm in thickness that were diluted with a quartz fraction in a horizontal quartz reactor (tube 2.5 mm in diameter). The gas flow was characterized by a developed turbulence, which increased as the linear velocity was increased to 1 m/s, while the microreactor was operated in a nearly plug-flow regime. The most typical results for the cerium–gadolinium series are presented in Fig. 25, and those for a sample of the ceria–zirconia–lanthana series are shown in Fig. 26. In all runs at 800–880°C, oxygen was completely consumed. As a rule, the products of selective methane oxidation appeared only after oxygen disappeared completely from the gas phase. The exceptions were the most selective samples, Pt/Ce–Zr–La (Fig. 26), which afforded hydrogen and CO even in the presence of oxygen. Depending on the oxidizing power of the surface and oxygen mobility, the catalysts can be divided into two groups. For the Pt/Ce–Pr–O samples and the $Pt/Ce_{0.8}Gd_{0.2}$ sample, which is characterized by the highest oxygen mobility in the lattice (see above), the reaction products contain a large amount of water and carbon dioxide and methane consumption is incomplete (Fig. 25a). This implies that on these catalysts, a considerable portion of methane turns into water and CO_2 and steam and dry reforming then take place. These samples are characterized by rather long relaxation times (during 70 min; see isotherms at 880°C), resulting in an increase in methane conversion and in synthesis gas selectivity. This is likely to be due to the fact that the surface of the initially oxidized samples comes to a steady state.

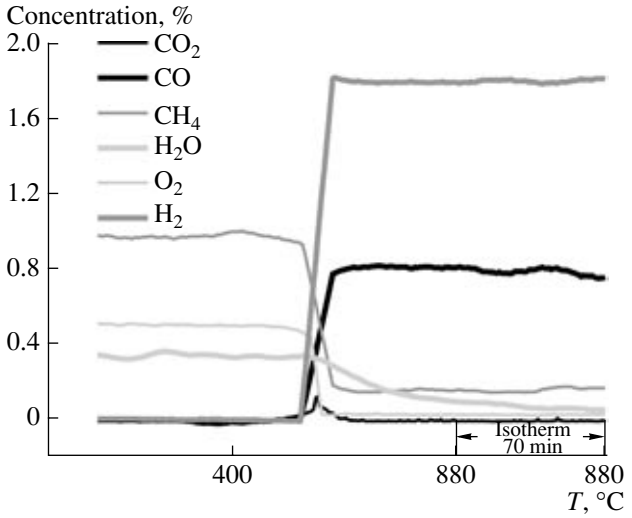

Fig. 26. Temperature-programmed reaction data for selective oxidation of methane on the platinum promoted sample $Ce_{0.4}Zr_{0.4}La_{0.2}O_{2-x}$ after oxygen treatment. Mixture composition is 1 vol % CH_4 + 0.5 vol % O_2 in He, contact time is 5 ms, and heating rate is 5 K/min.

As the contact time (τ) is shortened, a sharp decrease in conversion and hydrogen concentration is observed at progressively smaller changes in CO concentration (Fig. 27a). This implies that these samples are characterized by a high rate of after-oxidation of hydrogen resulting from methane dissociation, which is favored by the high oxygen concentration on the platinum particle surface [69] (due to diffusion from the support) and by the low activation energy of OH radical formation from H and O on platinum [70]. It is not impossible that methane dissociation on oxidized platinum surface itself involves an adsorbed oxygen atom [46]. The relatively weak change in CO and CO_2 selectivity formation with a change in τ can be explained by the parallel formation of these gases on the platinum surface [71].

At relatively long τ, high methane conversions and synthesis gas yields in the presence of these catalysts are apparently due to the secondary processes of steam and dry reforming. Indeed, after methane TPR, these systems are active in the reactions at $T = 880$°C and τ = 5 ms. However, one should take into account that the states of surface in selective oxidation and in methane steam/dry reforming differ because of the different compositions of the reaction mixture. Steam/dry reforming is characterized by a reduced state of the surface favoring highly efficient activation of both methane (on platinum) and soft oxidants H_2O/CO_2 (on the support). Therefore, it cannot be ruled out that the contribution of these processes to the overall conversion of methane during selective oxidation on catalysts of the first group is lower than follows from the comparison of methane conversion data for separate reactions.

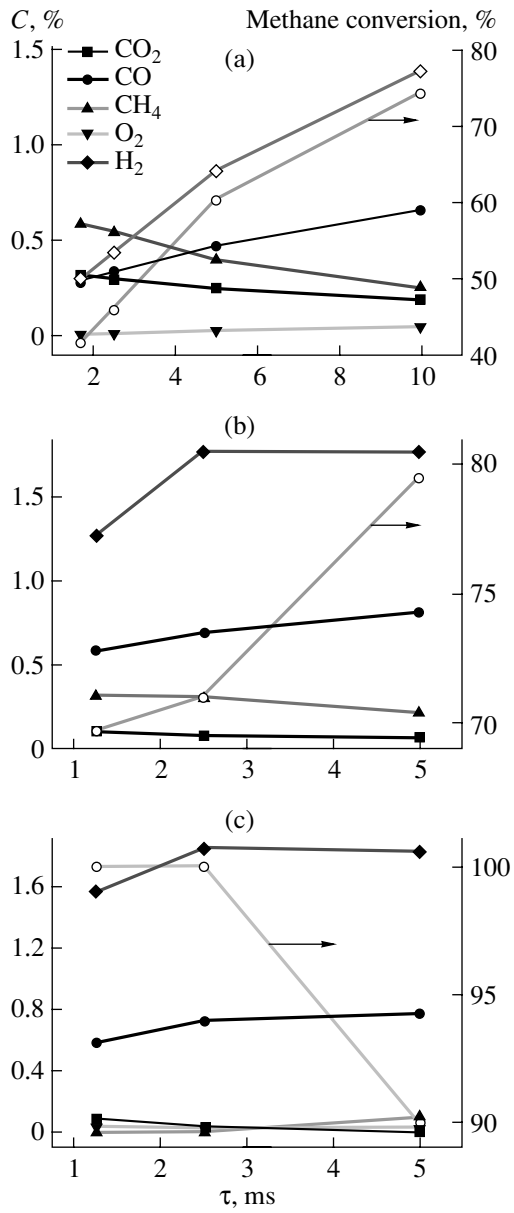

Fig. 27. Concentration (C) of components in the converted mixture versus contact time: (a) $Pt/Ce_{0.8}Gd_{0.2}O_{2-x}$, (b) $Pt/Ce_{0.6}Gd_{0.4}O_{2-x}$, and (c) $Pt/Ce_{0.4}Zr_{0.4}La_{0.2}O_{2-x}$. The initial composition of the mixture is 1 vol % CH_4 + 0.5 vol % O_2 in He. $T = 880$°C.

The other group includes some samples of the Pt/Ce–Zr–La–O and Pt/Ce–Gd–O systems characterized by lower oxygen mobility and lower oxidizing power of the surface. With these catalysts, the yield of deep oxidation products is lower, while methane conversion is higher (Figs. 25b, 26). Furthermore, these catalysts are characterized by a more rapid establishment of stationary concentrations of CO and hydrogen in the products. The selectivity of formation of the partial oxidation products insignificantly changes with a decrease in τ (Figs. 27b, 27c). This indicates that the

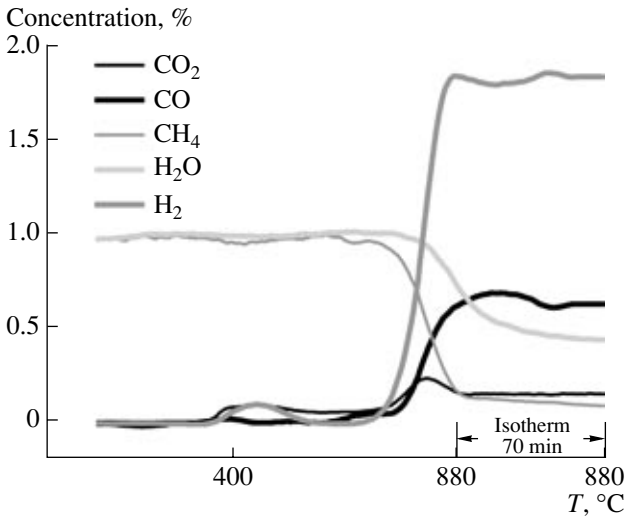

Fig. 28. Temperature-programmed reaction data for steam reforming of methane on the platinum promoted sample $Ce_{0.6}Gd_{0.4}O_{2-x}$ after selective methane oxidation on the same sample. Contact time is 5 ms, and heating rate is 5 K/min.

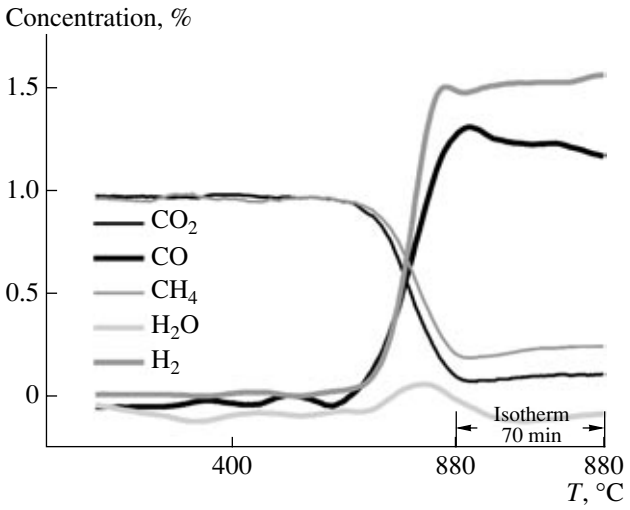

Fig. 29. Temperature-programmed reaction data for dry reforming of methane on the platinum promoted sample $Ce_{0.6}Gd_{0.4}O_{2-x}$ after selective oxidation and steam reforming of methane were successively carried out on the same sample. Contact time is 5 ms, and heating rate is 5 K/min.

reaction is dominated by the direct oxidation of methane to synthesis gas, including methane dissociation on platinum particles with selective oxidation of CH_x fragments by oxygen migrating from the support surface to the perimeter of the metallic particles. In the case of the Pt/Ce–Zr–La–O catalyst, hydrogen concentration even increases as the contact time is shortened within a certain interval, suggesting that the rate constant of hydrogen after-oxidation is not very high. As a result, the remaining oxygen is consumed in methane oxidation, increasing its conversion. At the same time, in the presence of these samples at 880°C, dry and steam reforming reactions at $\tau = 5$ ms also provide an equilibrium conversion of methane (see, e.g., Figs. 28 and 29 for the $Pt/Ce_{0.6}Gd_{0.4}O_{2-x}$ sample), indicating their high rate. Thus, unambiguous conclusions cannot be drawn concerning the route of selective oxidation by comparing the rate of selective methane oxidation with oxygen with the rates of steam and dry reforming on these catalysts at 880°C. Platinum supported on alumina at temperatures below 750°C, unlike rhodium, is not active in the steam and dry reforming of C_2–C_3 paraffins but is highly efficient in their selective oxidation into synthesis gas via the direct route [72]. Comparison with our results suggests that it is precisely the fluorite-like oxide supports that provide a high efficiency of platinum in steam and dry reforming. At the same time, the weak dependence of hydrogen selectivity on contact time [72] shows (Fig. 30) that the route of direct methane oxidation into synthesis gas is predominant for platinum supported on certain fluorite-like mixed oxides. The contributions of different routes are determined by the mobility of surface oxygen and its reactivity, which depends, in turn, on the chemical composition of the support. Obviously, the mobility and reactivity of surface oxygen should be optimized for particular process conditions (concentration of hydrocarbons and their nature, temperature, space velocity, and the presence of oxygen in the gas phase). Indeed, as follows, for example, from the above data, as the gadolinium content of cerium dioxide changes, oxygen mobility in the lattice passes through a maximum and the selectivity of formation of the selective methane oxidation products passes through a minimum.

Supported samples. The effect of the composition of the complex active component and pretreatment conditions on the activity of catalysts under isothermal conditions and selectivity of synthesis gas formation from methane was studied in detail for fluorite-like ceria–zirconia systems promoted with platinum, nickel, and nickel + platinum and for perovskite-like systems (lanthanum nickelate) supported on corundum (including corundum containing admixtures of transient modifications of alumina) [20–26]. Experiments were carried out on both a catalyst fraction and an individual triangular fragment of the channel of the monolith catalyst placed in a quartz reactor. Interaction with the support was shown to exert a strong effect on the reactivity of oxygen of the complex oxide systems and on the selectivity of synthesis gas formation.

The results of typical experiments on a fragment of a monolith with an active component containing nickel on a mixed oxide support are shown in Fig. 31. These systems are promising for frontal parts of monolith catalysts due to their resistance to evaporation under oxidative conditions as in the presence of nickel oxide and, especially, perovskite systems. Moreover, the frontal part contains oxygen, which prevents the carbon build-

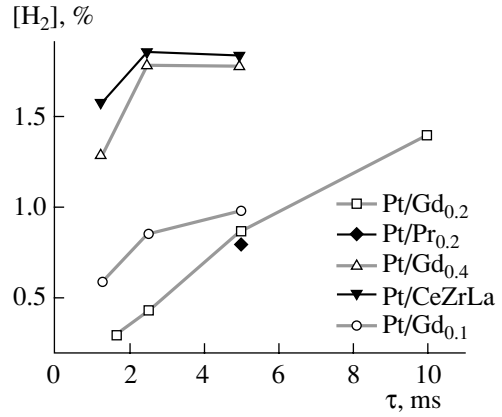

Fig. 30. Hydrogen concentration in the products of selective methane oxidation on the platinum-promoted fluorite-like oxide systems versus contact time. The initial composition of the mixture is 1 vol % CH_4 + 0.5 vol % O_2 in He (880°C).

up typical of nickel-containing catalysts [15]. In these experiments, a fragment of the monolith channel, being a hollow trihedral prism 10 to 30 mm in length, with a base side of 2.5 mm and a wall thickness of 0.3 mm, was placed in a quartz tubular reactor with an internal diameter of 4 mm. The entire space between the tube wall and channel was filled with silica fiber to provide for contact of the reaction mixture with the internal surface of the channel alone. Due to boundary effects and the small lengths of the fragments, gas flow through the channel was transient between laminar and turbulent.

As follows from the data presented in Fig. 31, the monolith systems operate rather efficiently at millisecond contact times even after oxidative treatment. It is most likely that the active component is rapidly reduced in the reaction medium to form dispersed metallic nickel particles bound to the complex fluorite- or perovskite-like oxide support. As in the case of the platinum-containing active component, the high efficiency of these systems is due to the conjugation of methane dissociation on metal (nickel) with the diffusion, over the surface, of reactive oxygen species capable of selectively oxidizing CH_x fragments to form synthesis gas. The weak dependence of methane conversion and CO selectivity on contact time at high temperatures suggests that the nickel-containing active component also favors the direct route of selective methane oxidation to synthesis gas. A substantially sharper dependence of the selectivity of formation of partial oxidation products on contact time is observed at lower temperatures. This implies that another, consecutive mechanism of the process is realized under these conditions in the presence of the nickel-containing active component. This mechanism includes methane combustion in the frontal part of the channel followed by the dry and steam reforming of the remaining hydrocarbon in the central or tail part of the fragment. Evidently, this route is favored by the high selectivity of nickel on the complex oxide support in the reactions of dry and steam methane reforming [72–74]. In this case, the rapid removal of carbon atoms resulting from methane dissociation from the nickel surface can occur through interaction with either lanthanum hydroxocarbonate fragments decorating nickel particles [74] or mobile hydroxyl groups of the support.

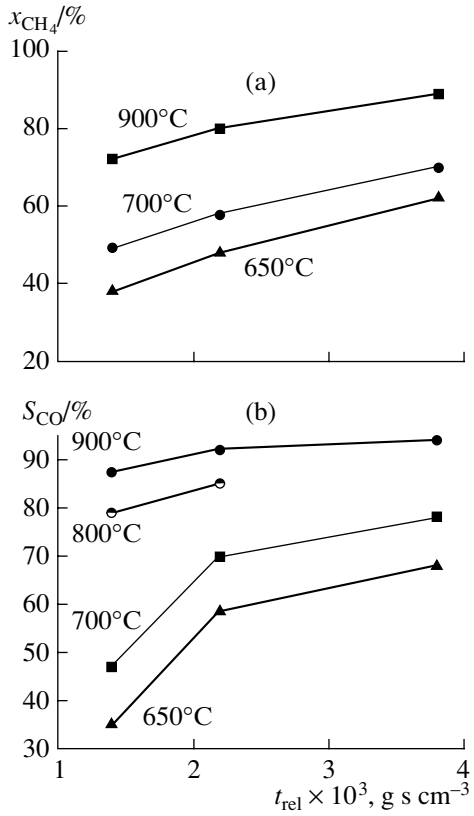

Fig. 31. (a) Methane conversion and (b) CO formation selectivity versus contact time and temperature. The ratio of contact time to the amount of active component (t_{rel}) was varied by changing the channel length: 31, 18, and 10 mm. Catalyst composition is 7 wt % $LaNiO_3$/10 wt % $Ce_{0.2}Zr_{0.8}O_2/\alpha$-$Al_2O_3$. Mixture consumption rate is 300 ml/min, and feed composition is 1 vol % CH_4 + 0.5 vol % O_2 in He.

It is important from a practical standpoint that, even at millisecond contact times, the efficiency of a complex active component supported on a ceramic monolith is not lower than the activity of bulk samples. This implies that, for these systems, there is no loss of activity in passing from the bulk to supported active components. An additional advantage of supported active components is their higher resistance to slow recrystallization and sintering processes at high temperatures, which are typical of selective hydrocarbon oxidation to synthesis gas at short contact times.

2. Development of New Types of Monolith Support

2.1. Monolith ceramic support of honeycomb structure [18, 24, 28, 37, 38]

The typical view of monolith supports is shown in Fig. 32. These supports have a wall thickness of 0.2–

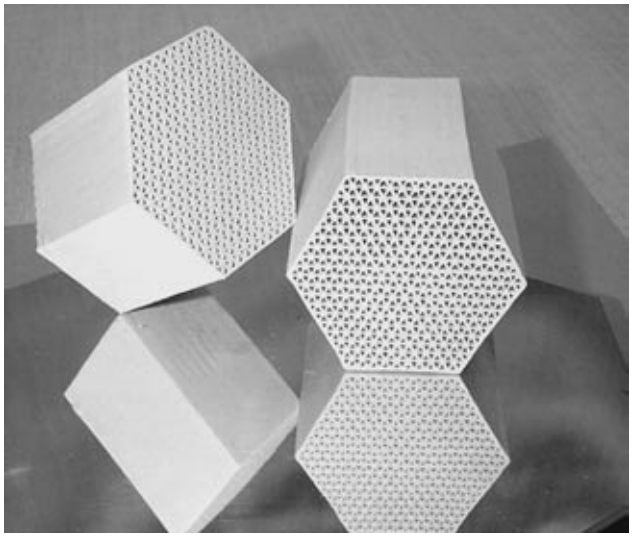

Fig. 32. Typical view of ceramic monolith supports developed at the Boreskov Institute of Catalysis, Siberian Division, Russian Academy of Sciences.

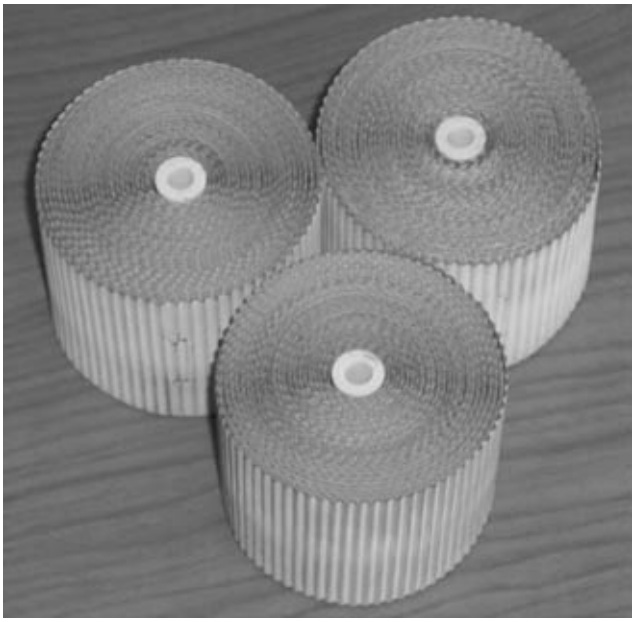

Fig. 33. Typical view of monolith supports based on foils of a thermally stable alloy.

0.3 mm and a triangular channel with a side of 2.3–2.5 mm and a hexagon side of 40 mm. They can be produced from either pure corundum or composite ceramic materials by incorporation of compounds with a low thermal expansion coefficient (aluminum titanate, titanum zirconate, and framework aluminosilicates) and partially stabilized zirconium dioxide. Catalysts are obtained by plastic extrusion of pastes containing both a ceramic material and a binder based on aluminum hydroxide. Production of such monolith supports includes drying under controlled conditions and calcination. Depending on calcination temperature and ceramic composition, the specific surface area of monoliths can vary from 5 to 100 m^2/g. Supports of this type are primarily designed for use in stationary synthesis gas generators of enhanced capacity with a large (>100 l) monolith loading and a relatively small number of on/off switches per run. Active components including both mixed oxides and platinum-group metals are supported by successive impregnation with appropriate solutions followed by drying and calcination. Preparation of this type of catalyst is detailed in a recent publication [24]. Pilot batches of monolith catalysts for selective oxidation and steam–air autothermal reforming of natural gas (trade mark IK-6-10) are produced at the Boreskov Institute of Catalysis, Siberian Division, Russian Academy of Sciences.

2.2. Monolith heat-conducting supports based on thermally stable metallic foils [26, 28, 29, 40, 44, 45]

The typical view of such monolith supports is shown in Fig. 33. Thermally stable alloys, such as Fechralloy and others, are used as materials for producing foils 20 to 50 μm in thickness. The foil surface is additionally protected from oxidation and/or undesirable contact with synthesis gas by coating it with a protective nonporous film of thermally stable oxides, a few microns in thickness, using the unique technology of blast dusting, which was developed at the Lavrent'ev Institute of Hydrodynamics, Siberian Division, Russian Academy of Sciences [75]. Monolith supports are obtained by stacking planar and corrugated foil strips followed by their winding to form an Archimedes spiral. Depending on the size of triangular channels, the density of cells varies from 200 to 400 per square inch. These supports are primarily designed for mobile synthesis gas generators, where a rapid startup and resistance to thermal and mechanical shocks are of special significance. The high thermal conductivity of these supports provides an efficient conjugation of exothermic and endothermic processes in different parts of the monolith, which makes it possible to achieve a high productivity and, hence, small dimensions of synthesis gas generators. In addition, the electric conductivity of these supports in combination with a proper stability of the dusted insulating layer allows rapid heating of the catalyst by passing electric current. This provides steady-state autothermal conditions for the selective oxidation of methane to synthesis gas within 1–2 min at contact times of 0.1–0.03 s and room temperature of the feed. Our studies on the design of these supports were first reported at the All-Russia Conference on Fuel Cells in July 2003 [28, 29]. Monolith catalysts for selective oxidation of natural gas to synthesis gas on metallic supports with

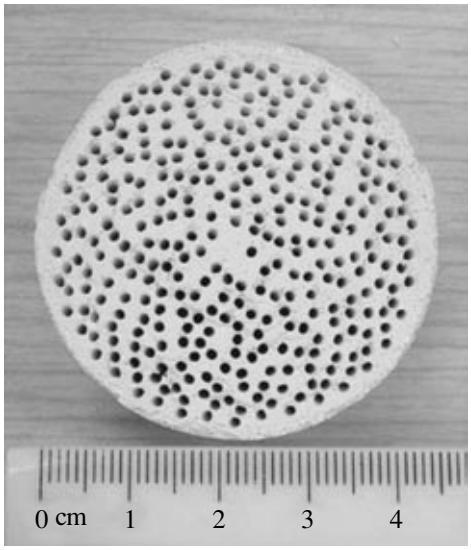

Fig. 34. Typical view of monolith microchannel supports.

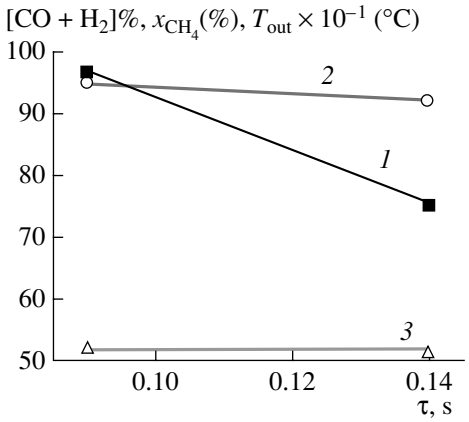

Fig. 35. (*1*) Temperature at the outlet of the monolith (T_{out}), (*2*) methane conversion (x_{CH_4}), and (*3*) sum of the CO and H_2 concentrations (converted to dry gas) versus contact time (τ) (the monolith volume is constant, while the mixture flow rate is varied). The natural gas-to-air ratio is $CH_4 : O_2 = 2$.

similar activity and electric startup characteristics were later reported by Korean researchers [76].

Introduction of an active component into these materials includes deposition of a secondary support of mixed fluorite-like oxides with the required oxygen mobility (see above) from an aqueous suspension containing an alumina-based binder. Next follows supporting of platinum-group metals and/or nickel, including perovskite-like precursors.

2.3. Microchannel supports based on heat-conducting cermets [28, 29, 35, 39, 41, 42]

The typical view of these supports is shown in Fig. 34. These microchannel supports are obtained by hydrothermal treatment of a mixture of aluminum powder and required compounds (oxide, metallic, carbide, etc., including those catalytically active in the desired reaction) in a special shaping matrix [77, 78]. In order to turbulize the reaction mixture flow, a system of intersecting axial and coiled microchannels of controlled configuration is formed by introduction of special elements burning upon high-temperature (to 1400°C) annealing of monoliths subsequent to hydrothermal treatment. Supports of this type have a high thermal conductivity and mechanical and thermal stability. They are primarily intended for applications that require minimization of undesirable gas-phase soot-producing reactions (during liquid fuel processing) or methane dimerization products (as in the selective oxidation of natural gas under pressure). It is most efficient to place these catalysts in the frontal part of the catalytic monolith, where the temperature can exceed 1300°C within the short start-up period of the synthesis gas generator.

An active component or its precursor is introduced into monolith supports of this type at the hydrothermal stage. When necessary, the active component or promoter is introduced by incipient wetness impregnation of a support with appropriate salt solutions.

3. Main Parameters of the Oxidative Reforming of Hydrocarbons into Synthesis Gas

3.1. Natural gas

Individual monoliths or their combinations (2 to 4 monoliths that may differ in both the type of support and the characteristics of the active component) are generally tested using real mixtures (stoichiometric natural gas–air mixtures) in the so-called "autothermal" regime [3]. A monolith(s) in combination with thermal screens (corundum or cordierite thin-wall supports) are placed in front of and behind the active monoliths in a flow reactor equipped with heating coils for partial compensation of the heat loss [79, 80]. To prevent the slippage of the reaction mixture between the reactor walls and monoliths and to reduce heat loss, the monoliths are tightly coated with ceramic fibrous materials. The feed is heated to a certain "ignition" temperature; after that, a steady state is established within tens of minutes. For ceramic supports, this state is characterized by a substantial difference in temperatures (250–300°C) between the frontal part and the rear end of the monolith up to 50 mm in length. As a rule, an increase in inlet temperature increases the monolith temperature and natural gas conversion. At a fixed inlet temperature, an increase in mixture consumption (shortening of the contact time) also increases the monolith temperature (Fig. 35) due to the relative decrease in heat losses,

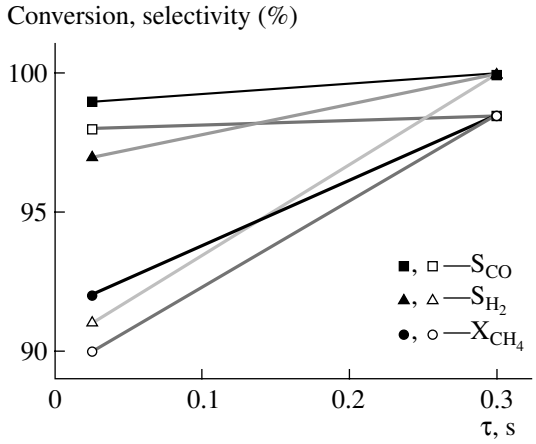

Fig. 36. Selective oxidation of the stoichiometric mixture of natural gas and air (CH_4 : $/O_2$ = 2) on the monolith catalysts (light points) 2 wt % Rh/α-Al_2O_3 and (dark points) IK-6-10 catalyst at 850°C.

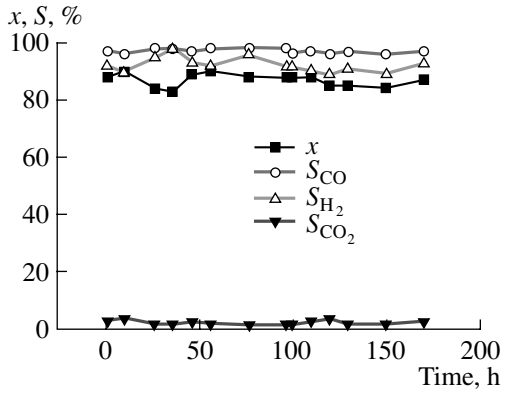

Fig. 37. Parameters of the selective oxidation of natural gas on the catalyst IK-6-10 at 850°C. Contact time is 0.03 s, and mixture composition is $CH_4/O_2/He$ = 2 : 1 : 5. After 110 h, ethane (5 vol %) was added to the mixture.

which is usually accompanied by an increase in hydrocarbon conversion and synthesis gas yield. In the autothermal regime, use of compensating coils and control of feed temperature make it possible to achieve an approximately constant monolith temperature despite the variation of contact time or the variation of temperature at the same contact time. To illustrate the typical effect of contact time at an approximately constant monolith temperature, we present in Fig. 36 some characteristics of the selective oxidation of natural gas into synthesis gas on a monolith catalyst (IK-6-10 containing mixed oxides promoted with a small amount of platinum-group metals) and on a catalyst containing 2 wt % rhodium on corundum. As follows from these data, the catalyst with the complex active component is more efficient, especially at short contact times. The levels of conversion and synthesis gas yield achieved with the monolith catalyst are similar to those achieved both with bulk metal oxide active components and with similar active components supported on an individual channel of a ceramic monolith for dilute model mixtures (see above). This implies that the preparation of monoliths allows one to prevent activity losses associated with the interaction between the active component and the support, unfavorable distribution of the active component over the monolith, deactivation of the active component because of carbon build-up at high methane concentrations in the mixture, and other undesirable phenomena [24].

One of the most important problems in catalyst design is to ensure resistance to carbon build-up, especially in the case of long-term contact between the catalyst and a real natural gas–air mixture containing heavier hydrocarbons. The catalysts of this type retained high activity and selectivity over up to 200 h in tests conducted in natural gas containing up to 5 vol % of ethane (Fig. 37). Moreover, catalysts containing fluorite-like solid solutions based on the ceria–zirconia system retain a stable activity level even when sulfur compounds in amounts up to 100 ppm are present in the reaction mixture [24]. Adding water or carbon dioxide to the original natural gas mixture makes it possible to vary the CO/H_2 ratio in the products over a wide range even when the equilibrium composition of the converted mixture is achieved within a short contact time [24]. This fact is of practical interest, especially for the steam–oxygen autothermal reforming of natural gas.

The performance stability and efficiency of catalysts in the selective oxidation of natural gas under elevated pressures are also important for practical use. In this respect, monolith catalysts on both straight-channel and microchannel supports exhibit high efficiency (the equilibrium gas composition is attained at short contact times) without carbon buildup. The corresponding data for the catalyst on the microchannel support are presented in Fig. 38.

3.2. Liquid fuel

A model hydrocarbon (isooctane) and real gasoline available from Omsk Petroleum Refinery ($C_{7.2}H_{13.36}$) with a low sulfur content and a high arene concentration up to 40 wt % were used to study the performance of monolith catalysts in synthesis gas production from liquid fuel. The selective oxidation (air reforming) and steam–air autothermal reforming of isooctane have been studied [28, 29, 42–45]. The contact time in those experiments was no longer than 0.1 s. The experimental and calculated (equilibrium) plots of the concentration of selective isooctane oxidation products (converted to dry mixture) versus air : fuel ratio on the monolith microchannel catalysts containing both fluorite- and perovskite-like oxides with platinum-group metals (Pt, Rh, Ru) are compared in Fig. 39. As follows from these data, the catalyst allows equilibrium conversion

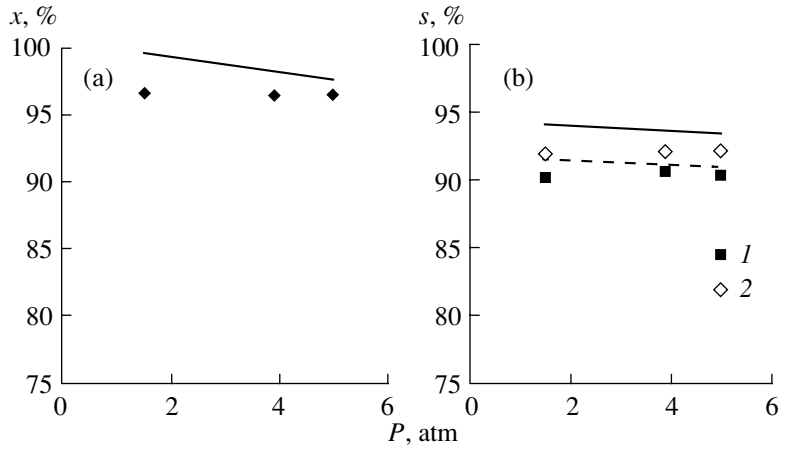

Fig. 38. (a) Natural gas conversion and (b) selectivities with respect to (*1*) CO and (*2*) H_2 for natural gas air reforming on the microchannel catalyst versus mixture pressure. The concentration of natural gas in the initial mixture is 25 vol %, the inlet temperature is 399°C, and contact time (under normal conditions) is 0.08 s. The composition of natural gas, vol %: methane, 90; ethane, 3.66; propane, 1.98; CO_2, 0.35; butanes, 0.7; and nitrogen, the balance. Points are experimental data, and lines are calculated equilibrium data.

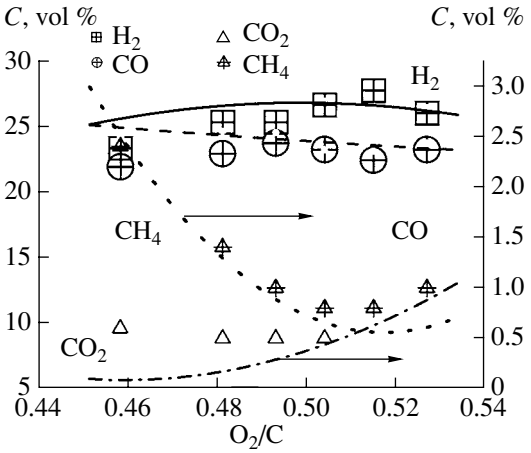

Fig. 39. Concentrations (*C*) of the products of isooctane selective oxidation on the monolith microchannel catalyst versus O_2 : C ratio in an isooctane–air mixture. The active components are $LaNiPt/CeO_2$ + Rh and Ru microadditives. Points are experimental data, and curves are calculated data. Isooctane consumption is 350 g/h, and air consumption ranges between 1.20 and 1.38 m^3/h. Contact time was varied between 0.094 and 0.108 s.

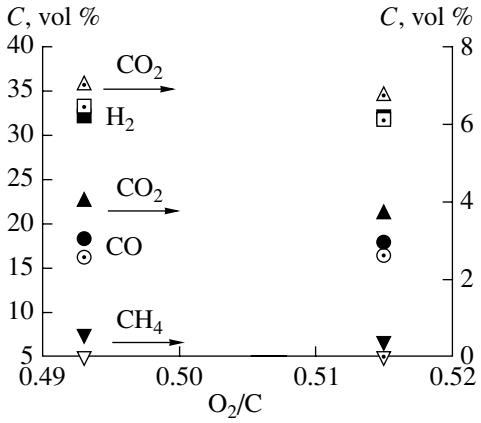

Fig. 40. Experimentally measured concentrations (*C*) of the (dark points) main components of synthesis gas and (light points) equilibrium data calculated for the autothermal reforming of isooctane on the monolith microchannel catalyst (O_2 : C = 0.494 and 0.515, H_2O : C = 0.81, and contact time is 0.07 s).

to be attained. Methane is the only hydrocarbon remaining in the products.

The high efficiency of this catalyst is retained in the steam–air autothermal reforming of isooctane (Fig. 40). In this case, the experimental CO_2 concentrations are approximately two times lower than the calculated values, and those of methane are higher (0.01 against 0.6%).

In the selective oxidation of gasoline into synthesis gas, the properties the Fechralloy foil catalyst with active components based on the lanthanum-stabilized ceria–zirconia oxide solid solution containing platinum-group metals were studied in detail [28, 29, 42–45]. Typical results are shown in Fig. 41. An almost complete conversion of the initial gasoline components was achieved in these experiments. In all cases, CO_2 content was below 0.5 vol % and no methane or other possible C_2–C_3 products were found within the sensitivity limit of the analytical method used. As follows from the data presented in Fig. 41, an increase in the air : fuel ratio (proportion of the exothermic component) brings together the inlet and outlet temperatures of the monolith catalyst. This means that the heat released in the inlet part of the monolith is efficiently transferred through the metallic support owing to its thermal conductivity, favoring endothermic reactions in

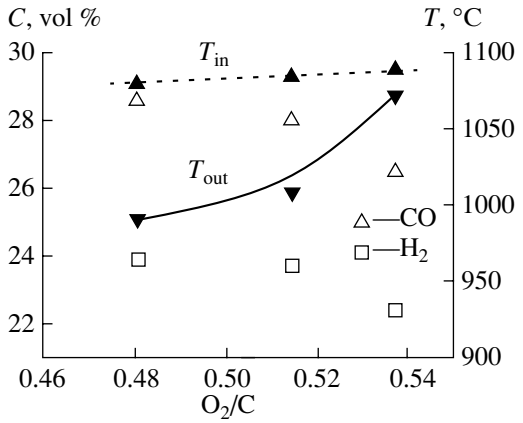

Fig. 41. Influence of the air-to-fuel ratio (as O_2 : C molar ratio) on the hydrogen and CO concentrations (C) in synthesis gas and (dark points) temperature at the inlet (T_{in}) and outlet (T_{out}) edges of the catalytic monolith for the selective oxidation of gasoline. Gasoline consumption is 0.893 kg/h, the support is Fechralloy, and the composition of the active component is LaNi(Pt + Ru).

the rear part. Therefore, metal-supported monolith catalysts are most promising for the selective oxidation and steam–air autothermal reforming of gasoline. No soot formation was observed at the process parameters examined when uniform fuel evaporation and perfect mixing with air were ensured.

CONCLUSIONS

The results presented in this review were obtained by long-term research in the area of monolith catalysts for selective oxidation and autothermal reforming of hydrocarbon fuels into synthesis gas. They show that progress in the development of efficient, stable, and rather cheap catalysts is due to employment of new types of active component and monolith support. A rather fruitful approach to design of the active component is based on combining platinum-group metals (Pt, Ru) and nickel, which can easily cleave a C–H bond in hydrocarbons, and mixed cerium-containing fluorite-like oxides with a high oxygen mobility in the lattice, which favors selective oxidation of activated hydrocarbon fragments into synthesis gas. Varying the composition of these oxide systems allows a smooth control of oxygen mobility to be performed in these systems. Therefore, their oxidizing power can be optimized for a particular composition of the reaction mixture, primarily taking into account the presence of oxygen. In some optimized systems, the efficient combination of the properties of the supported metal and oxygen-conducting support results in the domination of the direct selective hydrocarbon oxidation into synthesis gas and complete hydrocarbon conversion at millisecond contact times.

In the area of design of monolith supports for selective hydrocarbon oxidation into synthesis gas at short contact times, the development of heat-conducting supports based on thermally stable metallic foils or microchannel cermets made it possible to enhance heat transfer along the monolith and to decrease temperature gradients in monolith catalysts, especially for process startup, and thus prevent local overheating and raise thermal-shock resistance. Furthermore, efficient heat transfer over the monolith from the exothermic to endothermic zone increases the efficiency of hydrocarbon reforming. Conducting metallic supports can be heated by electric current, which provides a rapid startup of synthesis gas generators. This is especially important for automotive applications. The problem of increasing the service life of catalysts on monolith ceramic supports for high-capacity stationary synthesis gas generators was solved by introducing components with ultralow thermal expansion coefficients.

The catalysts developed showed a high efficiency in the selective oxidation and steam–air autothermal reforming of natural gas (including processes under pressure) and liquid fuel (including gasoline), affording equilibrium conversion under autothermal conditions at contact times of 0.03–0.1 s. They possess the high carbon buildup resistance necessary for their stable operation.

ACKNOWLEDGMENTS

This work was supported by INTAS (project no. 01-2162), the International Science and Technology Center (project no. 2529), RFTR (Sintez-gas Project), and the Siberian Division of the Russian Academy of Sciences (integration project nos. 17, 39, and 110).

We thank our colleagues from the Department of Physical Methods and the Department of Applied Catalysis of the Boreskov Institute of Catalysis, from the Institute of Solid-State Chemistry and Mineral Processing (Siberian Division, Russian Academy of Sciences), from the Lavrent'ev Institute of Hydrodynamics (Siberian Division, Russian Academy of Sciences), and from other institutions, including foreign ones, for their participation in experimental research, whose results have been included in separate publications and patents.

REFERENCES

1. Heinzel, A., Vogel, B., and Hubner, P., *J. Power Sources*, 2002, vol. 105, p. 202.
2. Ahmed, S. and Krumpelt, M., *Int. J. Hydrogen Energy*, 2001, vol. 26, p. 291.
3. Arutyunov, V.S. and Krylov, O.V., *Okislitel'nye prevrashcheniya metana* (Oxidative Conversion of Methane), Moscow: Nauka, 1988.
4. Krylov, O.V., *Katal. Prom–sti*, 2002, vol. 2, p. 16.
5. Bharadwaj, S.S. and Schmidt, L.D., *J. Catal.*, 1995, vol. 42, p. 109.

6. Recupero, V., Pino, L., Leonardo, L.D., Lagana, M., and Maggio, G., *J. Power Sources*, 1998, vol. 71, p. 208.
7. Krumpelt, M., Krause, T.R., Carter, J.D., Kopash, J.P., and Ahmed, S., *Catal. Today*, 2002, vol. 77, p. 3.
8. Cohn, D.R., Rabinovich, A., and Titus, C.H., *Int. J. Vehicle Design*, 1996, vol. 17, p. 550.
9. Wyszynski, J., *Int. J. Hydrogen Energy*, 1994, vol. 19, p. 557.
10. Kirwan, J.E., Greive, M.J., and Quader, A.A., *SAE Paper no. 012927*, 1999.
11. Kirwan, J.E., Greive, M.J., and Quader, A.A., *Proc. Global Powertrain Congress*, Stuttgart, 1999.
12. Kirwan, J.E., Greive, M.J., and Quader, A.A., *Proc. Global Powertrain Congress*, Detroit, 2000.
13. US Patent 6394791, 2002.
14. Lyubovsky, M., Smith, L.L., Castaldi, M., Karim, H., Nentwick, B., Etemad, Sh., LaPierre, R., and Pfefferle, W.C., *Catal. Today*, 2003, vol. 83, p. 71.
15. Freni, S., Calogero, G., and Cavallaro, S., *J. Power Sources*, 2000, vol. 87, p. 28.
16. O'Connor, R.P., Klein, E.J., and Schmidt, L.D., *Catal. Lett.*, 2000, vol. 70, p. 99.
17. O'Connor, R.P., Klein, E.J., Henning, D., and Schmidt, L.D., *Appl. Catal., A*, 2003, vol. 238, p. 29.
18. Isupova, L.A., Alikina, G.M., Tsybulya, S.V., Salanov, A.N., Boldyreva, N.N., Rusina, E.S., Ovsyannikova, I.A., Rogov, V.A., Bunina, R.V., and Sadykov, V.A., *Catal. Today*, 2002, vol. 75, p. 305.
19. Sadykov, V.A., Kuznetsova, T.G., Veniaminov, S.A., Kochubey, D.I., Novgorodov, B.N., Burgina, E.B., Moroz, E.M., Paukshtis, E.A., Ivanov, V.P., Trukhan, S.N., Beloshapkin, S.A., Potapova, Yu.V., Lunin, V.V., Kemnitz, E., and Aboukais, A., *React. Kinet. Catal. Lett.*, 2002, vol. 76, p. 83.
20. Parmon, V.N., Kuvshinov, G.G., Sadykov, V.A., and Sobyanin, V.A., *Stud. Surf. Sci. Catal.*, 1998, vol. 119, p. 677.
21. Pavlova, S.N., Sadykov, V.A., Paukshtis, E.A., Burgina, E.B., Degtyarev, S.P., Kochubei, D.I., Saputina, N.F., Kalinkin, A.V., Maximovskaya, R.I., Zaikovskii, V.I., Roy, R., and Agrawal, D., *Stud. Surf. Sci. Catal.*, 1998, vol. 119, p. 759.
22. Pavlova, S.N., Sadykov, V.A., Parmon, V.N., Bobrova, I.I., Zolotarskii, I.A., Kuzmin, V.A., Salanov, A.N., Bunina, R.V., Saputina, N.F., Snegurenko, O.I., and Vostrikov, Z.Yu., *EuropaCat V*, Limerick, Irekand, 2001, vol. 4, 5-O-04.
23. Simakov, A.V., Pavlova, S.N., Sazonova, N.N., Sadykov, V.A., Snegurenko, O.I., Rogov, V.A., Parmon, V.N., Zolotarskii, I.A., Kuzmin, V.A., and Moroz, E.M., *Chem. Sustainable Dev.*, 2003, vol. 11, p. 263.
24. Pavlova, S.N., Sadykov, V.A., Bobrova, I.I., Saputina, N.F., Snegurenko, O.I., Bunina, R.V., Salanov, A.N., Kuz'min, V.A., Vostrikov, Z.Yu., and Zolotarskii, I.A., *Katal. Prom–sti*, 2004, special issue, p. 12.
25. Pavlova, S.N., Sazonova, N.N., Sadykov, V.A., Snegurenko, O.I., Rogov, V.A., Zolotarskii, I.A., and Moroz, E.M., *EuropaCat VI*, Innsbruck, 2003, ISO 36.
26. Pavlova, S., Sadykov, V., Snegurenko, O., Vostrikov, Z., Tikhov, S., Zolotarskii, I., Kuzmin, V., Bobrova, L., and Ulianitsky, V., *EuropaCat VI*, Innsbruck, 2003, B3.097.
27. Kuznetsova, T.G., Sadykov, V.A., Moroz, E.M., Trukhan, S.N., Paukshtis, E.A., Kolomiichuk, V.N., Burgina, E.B., Zaikovskii, V.I., Fedotov, M.A., Lunin, V.V., and Kemnitz, E., *Stud. Surf. Sci. Catal.*, 2002, vol. 143, p. 659.
28. Sadykov, V.A., Pavlova, S.N., Bunina, R.V., Tikhov, S.F., Snegurenko, O.I., Kuznetsova, T.G., Alikina, G.M., Dyatlova, Yu.N., Lukashevich, A.I., Sazonova, N.N., Frolova, Yu.V., Zolotarskii, I.A., Bobrova, L.N., Kuz'min, V.A., Vostrikov, Z.Yu., Ul'yanitskii, V.Yu., Chaikina, M.V., and Avvakumov, E.G., *Vtoroi Vserossiiskii seminar po toplivnym elementam i energoustanovkam na ikh osnove* (Second All-Russia Workshop on Fuel Cells and Fuel-Cell-Based Power Plants), Novosibirsk, 2003, p. 191.
29. Bobrova, L.N., Korotkikh, V.N., Zolotarskii, I.A., Sadykov, V.A., Pavlova, S.N., Bunina, R.V., Snegurenko, O.I., Tikhov, S.F., Kuznetsova, T.G., Brizitskii, O.F., Terent'ev, V.Ya., and Khristolyubov, A.P., *Vtoroi Vserossiiskii seminar po toplivnym elementam i energoustanovkam na ikh osnove* (Second All-Russia Workshop on Fuel Cells and Fuel-Cell-Based Power Plants), Novosibirsk, 2003, p. 147.
30. Sadykov, V.A., Kuznetsova, T.G., Alikina, G.M., Potapova, Yu.V., Muzykantov, V.S., Rogov, V.A., Kriventsov, V.V., Kochubei, D.I., Moroz, E.M., Zaikovskii, V.I., Kolomiichuk, V.N., Paukshtis, E.A., Burgina, E.B., Zyryanov, V.V., Neophytides, S., and Kemnitz, E., *EuropaCat VI*, Innsbruck, 2003, A2.115.
31. Kuznetsova, T.G., Sadykov, V.A., Veniaminov, S.A., Alikina, G.M., Paukshtis, E.A., Kulikova, Yu.N., Moroz, E.M., Burgina, E.B., Rogov, V.A., Trukhan, S.N., Kolomiichuk, V.N., and Neophytides, S., *EuropaCat VI*, Innsbruck, 2003, ISO 22.
32. Sadykov, V.A., Kuznetsova, T.G., Alikina, G.M., Frolova, Yu.V., Lukashevich, A.I., Potapova, u.V., Muzykantov, V.S., Rogov, V.A., Kriventsov, V.V., Kochubei, D.I., Moroz, E.M., Zyuzin, D.A., Zaikovskii, V.I., Kolomiichuk, V.N., Paukshtis, E.A., Burgina, E.B., Zyryanov, V.V., Uvarov, N.F., Neophytides, S., and Kemnitz, E., *3rd Asia–Pacific Congress on Catalysis*, Dalian, China, 2003, vol. 1, p. 158.
33. Sadykov, V.A., Kuznetsova, T.G., Alikina, G.M., Frolova, Yu.V., Lukashevich, A.I., Potapova, Yu.V., Muzykantov, V.S., Rogov, V.A., Kriventsov, V.V., Kochubei, D.I., Moroz, E.M., Zyuzin, D.A., Zaikovskii, V.I., Kolomiichuk, V.N., Paukshtis, E.A., Burgina, E.B., Zyryanov, V.V., Uvarov, N.F., Neophytides, S., and Kemnitz, E., *Proc. X APAM Topical Seminar and III Conf. on Materials of Siberia: Nanoscience and Technology*, Novosibirsk, Russia, 2003, p. 378.
34. Sadykov, V.A., Isupova, L.A., Yakovleva, I.S., Alikina, G.M., Lukashevich, A.I., and Neophytides, S., *React. Kinet. Catal. Lett.*, 2004, vol. 81, p. 393.
35. Pavlova, S., Tikhov, S., Sadykov, V., Dyatlova, Y., Snegurenko, O., Vostrikov, Z., Zolotarskii, I., and Kuzmin, V., *Natural Gas Conversion VII*, Dalian, China, 2003.
36. Sadykov, V.A., Lunin, V.V., Kuznetsova, T.G., Alikina, G.M., Frolova, Yu.V., Lukashevich, A.I., Potapova, Yu.V., Muzykantov, V.S., Veniaminov, S.A., Rogov, V.A., Kriventsov, V.V., Kochubei, D.I., Moroz, E.M., Zyuzin, D.A., Zaikovskii, V.I., Kolomiichuk, V.N., Paukshtis, E.A., Burgina, E.B., Zyryanov, V.V., Uvarov, N.F.,

Neophytides, S., and Kemnitz, E., *Natural Gas Conversion VII*, Dalian, China, 2003.

37. RF Patent 2144844, 1997.
38. RF Patent 2204434, 2003.
39. RF Patent Application 2003130311, 2003.
40. RF Patent Application 2003130312, 2003.
41. RF Patent Application 2003130313, 2003.
42. RF Patent Application 2003130310, 2003.
43. RF Patent Application 2003130309, 2003.
44. RF Patent Application 2003130308, 2003.
45. RF Patent Application 2003130314, 2003.
46. Aghalayam, O.P., Park, Y.K., Fernandes, N., Papavassiliou, V., Mhadeshwar, A.B., and Vlachos, D.C., *J. Catal.*, 2003, vol. 213, p. 23.
47. Dong, W.-Sh., Jun, K.-W., Roh, H.-S., Liu, Zh.-W., and Park, S.-E., *Catal. Lett.*, 2002, vol. 78, p. 215.
48. US Patent 6110861, 2000.
49. Inaba, H. and Tagawa, H., *Solid State Ionics*, 1996, vol. 83, p. 1.
50. Narula, C.K., Allison, J.E., Bauer, D.R., and Gandhi, H.S., *Chem. Mater.*, 1996, vol. 8, p. 984.
51. Narula, C.K., Haack, L.P., Chun, W., Jen, H.-W., and Graham, G.W., *J. Phys. Chem. B*, 1999, vol. 103, p. 3634.
52. Choudhari, V.R., Rajput, A.M., and Rane, V.H., *Catal. Lett.*, 1993, vol. 22, p. 289.
53. Hayakawa, T., Harihara, H., Arnfinn, G.A., York, A.P., Suzuki, K., Yasuda, H., and Tekehira, K., *Angew. Chem., Int. Ed. Engl.*, 1996, vol. 35, p. 192.
54. Zhang, Zh. and Verykios, X., MacDonald S.M., and Affrossman, S., *J. Phys. Chem.*, 1996, vol. 100, p. 744.
55. US Patent 3330697, 1967.
56. Logan, A.D. and Shelef, M., *J. Mater. Res.*, 1994, vol. 9, p. 468.
57. *Catalysis by Ceria and Related Materials*, Trovarelli, A., Ed., London: Imperial College Press, 2002.
58. Sayle, T.X., Parker, S.C., and Catlow, C.R.A., *Surf. Sci.*, 1994, vol. 316, p. 329.
59. Bulgakov, N.N., Sadykov, V.A., Lunin, V.V., and Kemnitz, E., *React. Kinet. Catal. Lett.*, 2002, vol. 76, p. 111.
60. Hadjiivanov, K.I. and Vaysillov, T.N., *Adv. Catal.*, 2002, vol. 47, p. 2002.
61. Tsyganenko, A.A. and Filimonov, V.N., *Usp. Fotoniki*, 1974, no. 4, p. 51.
62. Petot-Ervas, G., Petot, C., Raulot, J.M., Kusinski, J., Sproule, I., and Graham, M., *Mat. Res. Soc. Symp. Proc.*, 2003, vol. 756, p. EE 4.4.1.
63. Muzykantov, V.S., *React. Kinet. Catal. Lett.*, 1987, vol. 35, p. 437.
64. Muzykantov, V.S., Kemnitts, E., Sadykov, V.A., and Lunin, V.V., *Kinet. Katal.*, 2003, vol. 44, p. 349.
65. Mamontov, E., Egami, T., Brezny, R., Koranne, M., and Tyagi, S., *J. Phys. Chem. B*, 2000, vol. 104, p. 11110.
66. Bulgakov, N.N., Sadykov, V.A., Lunin, V.V., and Kemnitz, E., *React. Kinet. Catal. Lett.*, 2002, vol. 76, p. 103.
67. Roh, H.-S., Jun, K.-W., Dong, W.-Sh., Park, S.-E., and Baek, Y.-S., *Catal. Lett.*, 2001, vol. 74, p. 31.
68. Richardson, J.T., Garrait, M., and Hung, J.-K., *Appl. Catal., A*, 2003, vol. 255, p. 69.
69. Weng, W.Zh., Yan, Q.G., Luo, Ch.R., Liao, Y.Y., and Wan, H.L., *Catal. Lett.*, 2001, vol. 74, p. 37.
70. Hickman, D.A. and Schmidt, L.D., *J. Catal.*, 1992, vol. 138, p. 267.
71. Basini, L., Aragno, A., and Vlaic, G., *Catal. Lett.*, 1996, vol. 39, p. 49.
72. Matsumura, Y. and Nakamori, T., *App. Catal., A*, 2004, vol. 258, p. 107.
73. Inui, T., *Catalysis*, 2002, vol. 16, p. 133.
74. Verykios, X.E., *Int. J. Hydrogen Energy*, 2003, vol. 28, p. 1043.
75. Barten'ev, S.S., Fed'ko, Yu.R., and Grigor'ev, A.I., *Detonatsionnye pokrytiya v mashinostroenii* (Antiknock Coatings in Machine Building), Leningrad: Mashinostroenie, 1982.
76. Jung, H., Yoon, W.L., Lee, H., Park, J.S., Shin, J.S., La, H., and Lee, J.D., *J. Power Sources*, 2003, vol. 124, p. 76.
77. Tikhov, S.F., Sadykov, V.A., Salanov, A.N., Potapova, Yu.V., Tsybulya, S.V., Litvak, G.S., and Pavlova, S.N., *Mater. Res. Soc. Symp. Proc.*, 1998, vol. 497, p. 200.
78. Tikhov, S.F., Sadykov, V.A., Bobrova, I.I., Potapova, Yu.V., Fenelonov, V.B., Tsybulya, S.V., Pavlova, S.N., Ivanova, A.S., Kruglyakov, V.Yu., and Bobrov, N.N., *Stud. Surf. Sci. Catal.*, 2001, vol. 136, p. 745.
79. Sadykov, V.A., Pavlova, S.N., Saputina, N.F., Zolotarskii, I.A., Pakhomov, N.A., Moroz, E.M., Kuzmin, V.A., and Kalinkin, A.V., *Catal. Today*, 2000, vol. 61, p. 93.
80. Pavlova, S.N., Sadykov, V.A., Frolova, Yu.V., Saputina, N.F., Vedenikin, P.M., Zolotarskii, I.A., and Kuzmin, V.A., *Chem. Eng. J.*, 2003, vol. 91, p. 227.